Title
Dysflective Cones in Healthy and Retinal Disease Eyes

Author
Bensinger, Ethan

Publication Date
2021

Peer reviewed|Thesis/dissertation

Dysflective Cones in Healthy and Retinal Disease Eyes

By
Ethan S. Bensinger

A dissertation submitted in partial satisfaction of the
requirements for the degree of
Doctor of Philosophy
in
Vision Science
in the
Graduate Division
of the
University of California, Berkeley

Committee in charge:
Professor Austin Roorda, Chair
Professor John G Flannery
Professor Ren Ng

Spring 2021

Dysflective Cones in Healthy and Retinal Disease Eyes

By Ethan Bensinger

ABSTRACT

Dysflective Cones in Healthy and Retinal Disease Eyes

by

Ethan S. Bensinger

Doctor of Philosophy in Vision Science

University of California, Berkeley

Professor Austin Roorda, Chair

Robust, sensitive measures of foveal health and cone loss, particularly ones that rely on structural measures rather than subjective and time consuming psychophysical measures, could facilitate measurement of disease progression. The research described in this document uses multimodal high-resolution imaging techniques to study the relationship between structure of cone photoreceptors and visual function in both healthy and diseased eyes.

Visualizing cone structure in living eyes offers a way to detect and monitor retinal disease and assess the health of cone photoreceptors. It is generally the case that regions that lack normal reflections from the photoreceptors correspond to regions that lack functional cones. However, areas of hyporeflective cones (cones that reflect significantly less than normal) even over large areas have been reported to have function, and these are defined as dysflective cones. The research described in this document focuses on determining the presence of these dysflective cones in healthy subjects, the timeline of dysflective cone reflectivity changes, and the sensitivity differences between healthy appearing cones and dysflective cones. Healthy dysflective cones were found to have similar function to surrounding areas, while dysflective areas in participants with retinal disease were found to have worse function, elevated thresholds, compared to surrounding areas.

TABLE OF CONTENTS

LIST OF FIGURES

LIST OF TABLES

LIST OF ABBREVIATIONS

AMD Age-related macular degeneration
AO Adaptive optics
AOM Acousto-optic modulator
AOMP Adaptive optics microperimetry
AOSLO Adaptive optics scanning laser ophthalmoscope (or ophthalmoscopy)
a.u. Arbitrary units
BCEA Bivariate contour ellipse area
BCVA Best corrected visual acuity
BM Bruch's membrane
CD Candela
CRD Cone Rod Dystrophy
COST Cone Outer Segment Tips
D Diopters
dB Decibels
ELM External limiting membrane
ERG Electroretinogram
ETDRS Early Treatment of Diabetic Retinopathy Study
FAF Fundus Autofluorescence
HSWS Hartmann-Shack wavefront sensor (or sensing)
IR Infrared
IS/OS Inner segment/outer segment
LCA Longitudinal chromatic aberration
MacTel Macular telangiectasia
MAIA Macular Integrity Assessment
MH Macular hole
OCT Optical coherence tomography
OCTA Optical coherence tomography angiography
OD Right Eye
OS Left Eye
PMT Photomultiplier tube
PRL Preferred retinal locus of fixation
PSF Point spread function
PTOS Posterior tip of the outer segment
RCD Rod Cone Dystrophy
RD Retinal detachment
ROI Region of interest
RP Retinitis pigmentosa
RPE Retinal Pigment Epithelium
SD Standard deviation
SD-OCT Spectral domain optical coherence tomographer (or tomography)
SLO Scanning laser ophthalmoscope (or ophthalmoscopy)
TCA Transverse chromatic aberration
Td Trolands
USH2A Usher's syndrome type 2A

ACKNOWLEDGEMENTS

First and foremost, I have to acknowledge my wife Christy Sheehy, without whom I wouldn't have been able to come close to finishing this dissertation. Christy, you inspire me every day to be a better person and a better scientist. Thank you to my dad for helping inspire a love of science at an early age, and my mom for being my rock through all my academic pursuits. Thank you to my sister, my earliest protector and cheerleader, and my grandparents for their love and support. Thank you to my whole family; my brother Jeremy, my uncles Mark and Greg for being there when I really need you all.

I have been blessed to have two advisors: Austin Roorda and Jacque Duncan. Austin has been my advisor at Berkeley, constantly pushing me to be a better, more critical scientist. Jacque has been my link to clinical science, allowing me to interface with patients and understand the inner workings of retinal disease. Maybe most critically, the Roorda lab has the best and most supportive engineer in Pavan Tiruveedhula, who no Roorda lab student could get anything else done without. Also thank you to Ally Boehm, a fantastic friend and lab mate. I am grateful to the whole of Roorda lab: Katharina Foote, Yiyi Wang, Swati Bhargava, Ram Sabesan, Will Tuten, Kavitha Ratnam, Brian Schmidt, Sanam Mozaffari, Francesco LaRocca, Volker Jaedicke, Nicolas Bensaid, and Norick Bowers. I am also extremely lucky to have worked with the Duncan team; Arshia Mian, Nic Rinella, Janette Tang, Mary Lew, Kolawole Olubayo, and especially Jessica Wong who helped make this data possible. Thanks to the clinical science learned with these two labs and my new mentor found in Mark Abelson I am exceedingly hopeful for my future scientific career.

Chapter 1 | Introduction

1.1 Retinal Anatomy and the Effect on Visual Perception

Vision provides a vital sense for navigating the world and requires the entire visual pathway to be in working order, from light entering the eye all the way to the brain for processing. Light enters the eye and is focused by the cornea and then the lens due to their refractive power. These two surfaces focus the light on the retina in an emmetropic eye but have optical aberrations that can cause light to blur on the retina. The light passes through the transparent neural layers of the retina and is sensed by the rod and cone photoreceptors' photopigments, rhodopsin and opsin respectively; they provide the critical first response to light. Underneath the cones lies the retinal pigment epithelium (RPE) cells which nourish the cones in conjunction with the underlying choroidal blood vessels and the capillaries of the choriocapillaris.

Photoreceptor cells sense light through photoisomerization in the photoreceptor opsins and polarize leading to a cascading signal sent through transparent neural layers. Photoreceptors were first discovered to be light sensitive by Franz Boll and Willy Kllhne who observed retinal pigments in the living frog retina (Boll, 1876), but it wasn't until later that the biochemical process of phototransduction was elucidated by George Wald (Wald 1955). The phototransduction process causes photoreceptors to have the highest oxidative metabolism in the entire body, requiring immense blood flow within the choroid (Wright et al., 2010). Due to photoreceptors high oxidative stress, diseases causing structural changes to any of the underlying supportive layers of the retina, or affecting any part of the visual cascade, can cause disruptions to vision.

Photoreceptors are broken up into two classes: cones, which provide photopic high spatial resolution vision and color vision, and rods, which provide scotopic vision and motion perception. Rod photoreceptors have a peak sensitivity at 498nm and outnumber cones at 92 million compared to only 4.6 million cones. Figure 1.1 shows the peak sensitivity of rods and the 3 types of cones. Cones are typed by the wavelength that each cone opsin is most sensitive to: S cones with a sensitivity peak at 420nm, M cones with a sensitivity peak at 534nm, and L cones with a sensitivity peak of 564nm (Bowmaker & Dartnall, 1980).

Both rod and cone photoreceptors are made up of an inner segment, which contains the cell nucleus, the mitochondria, and connects to the cone synapse, and the outer segment, which contains discs containing the photosensitive opsin. The outer segment discs are shed through phagocytosis of the RPE at the outer segment tip and are renewed by the inner segment near the inner segment/outer segment junction (IS/OS).

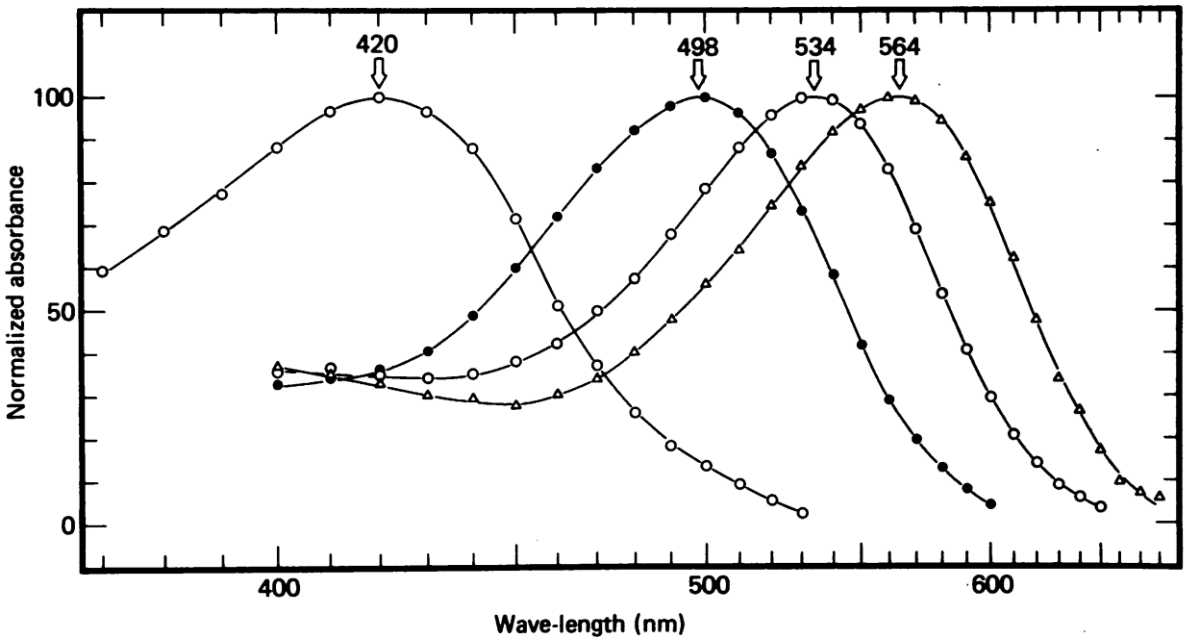

Figure 1.1 Absorbance spectra of rods (filled in circles peak at 498nm), and cone outer segments (s cones peak at 420nm, m cones peak at 534nm, and L cones peak at 564nm). Adapted from Bowmaker and Dartnall 1980.

Once light is sensed by the photoreceptors, the signal is passed through the transparent neuronal layers ending in the ganglion cells whose axons exit through the optic nerve head. At the optic nerve there is a "blind spot", an area where there are no photoreceptors and where the brain interpolates or fills in this area based on the surroundings. This process of filling in from the surroundings also occurs for areas of photoreceptor atrophy, i.e. areas with completely disrupted photoreceptors that provide no function(Zur & Ullman, 2003).

Fifteen visual degrees from the optic nerve is the fovea, the area with the highest density of cone photoreceptors. Within the central 1.5 degrees of the fovea, cone photoreceptors are tightly packed so that cones at the very center about ½ a minute of visual angle. It is the size of these cone photoreceptors that help govern the smallest perceivable stimuli. This dense packing of cones and their 1:1 connection to ganglion cells makes it the perfect area for the preferred retinal locus (PRL), which is the area used for fixating on a stimulus. Rod photoreceptors begin to outnumber cones with increasing eccentricity, while cones enlarge with multiple cones connecting to single ganglion cells (Curcio et al., 1990).

1.2 Adaptive Optics

1.2.1 Methods of Adaptive Optics Imaging

Imaging individual cone photoreceptor structure in living eyes near the fovea requires the correction of optical aberrations within the imaging system. Even when the optics of the eye are corrected with glasses to account for defocus and astigmatism, there are still higher order aberrations that prevent diffraction limited imaging of the retina. Adaptive optics measures optical aberrations using a wavefront sensor and converts the wavefront information into voltage signals for the actuators of a deformable mirror to push and pull in order to compensate for the aberrated wavefront. The adaptive optics scanning laser ophthalmoscope (AOSLO) system is a

point scanning laser system that uses adaptive optics and achieves near diffraction limited imaging of the individual cone photoreceptors at their smallest packing in the fovea (Liang et al., 1997; Roorda et al., 2002; Y. Wang et al., 2019).

This high-resolution retinal imaging capability measures the cones' intrinsic ability to reflect light. A confocal pinhole of the AOSLO system is placed directly before the detector in a plane conjugate to the retina to reject out of focus light improving contrast and axial resolution (Webb et al., 1987). The confocal AOSLO set up provides the system with a resolution of approximately 2.5 μm lateral and <100 μm axial (Roorda et al., 2002). With the confocal pinhole placed in the retinal plane, a PMT records the back reflected light that emanates from the two junctions of photoreceptors with the highest refractive index change: the IS/OS junction and the outer segment tip junction with the RPE apical processes (Kocaoglu et al., 2011).

Recent developments have led to non-confocal imaging modalities that can image different retinal structures using multiply scattered light. This multiply scattered light occurs because not all light is directly backscattered from the retina to the pupil. Instead, some light is scattered forward by other structures in the retina and then scattered back toward the pupil as shown in Figure 1.2A (Burns et al., 2019). With non-confocal AOSLO imaging, it is possible to image in vivo previously unseen structures and individual cells within the retina as shown in Figure 1.2B. These structures include the retinal pigment epithelium layer (Carroll et al., 2013), the cone inner segments (Scoles et al., 2014), ganglion cells (Ethan A. Rossi et al., 2017), and individual red blood cells (Joseph et al., 2018).

In photoreceptors, by subtracting signals of two incoherent PMT's the multiply scattered light focuses on the cone inner segments (Scoles et al., 2014). This subtraction provides focus on the cone inner segments because the cell body of the inner segments acts as a lens due to their higher refractive index, causing light to deviate laterally in opposite directions for each side of the non-confocal apertures (Guevara-Torres et al., 2020).

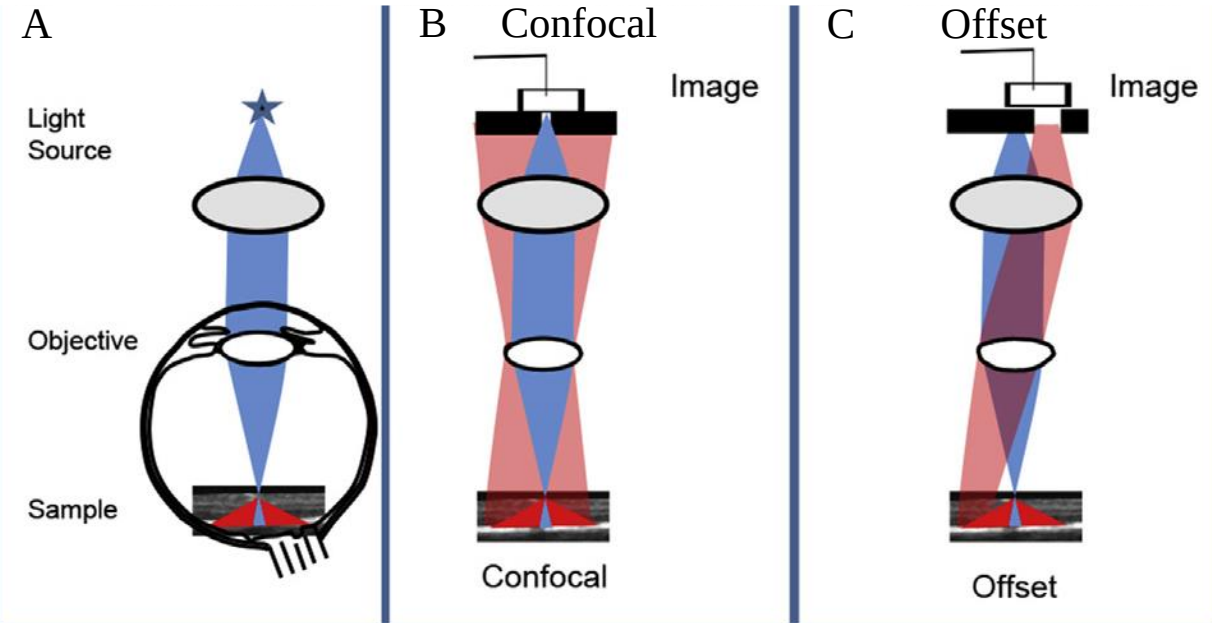

Figure 1.2 A Model illustrating offset aperture imaging. In blue is the incoming light and the red shows the multiply scattered light path and back reflectance. Adapted from Burns et al.

2019.

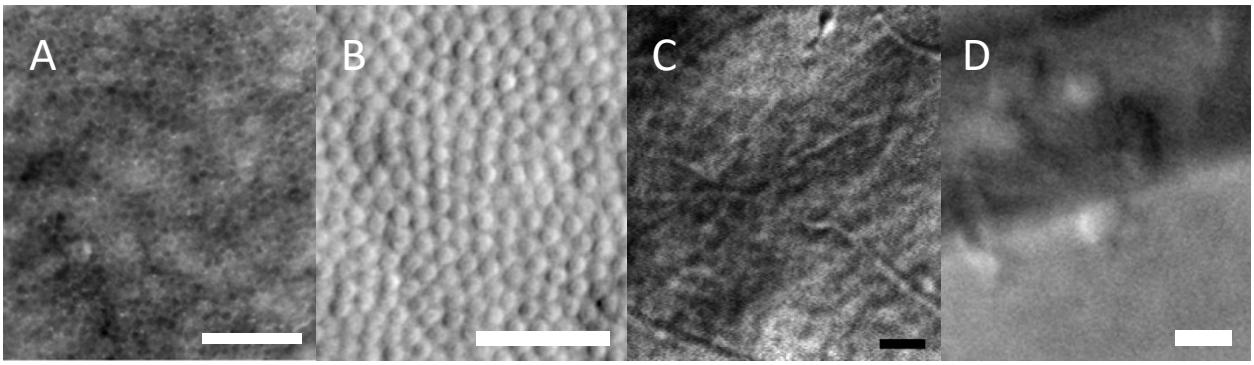

Figure 1-2B Offset aperture AOSLO imaging of different structures in the human retina. A shows RPE bullet hole appearance in the fovea with dark field imaging i.e. offset aperture incoherent imaging adapted from Scoles et al. 2013. Scale bar is 100µm. B shows cone inner segments at 5 degrees eccentricity from the fovea using split detector imaging adapted from Scoles et al. 2014. Scale bar C shows ganglion cells measured with multi-offset imaging at 12 degrees from the fovea adapted from Rossi et al. 2017. Scale bar is 50µm. D shows individual immune cells in mouse retinal vessels. Scale bar is 10µm.s

1.2.2 Adaptive Optics Microperimetry

Adaptive optics microperimetry (AOMP) provides measurements of visual sensitivity with diffraction limited stimuli locked onto the retina. AOMP provides functional measurements of AOSLO cone photoreceptor structure via small spot stimuli, down to the size of a single foveal cone. To correctly target a particular area, high speed retinal tracking and measurements of chromatic aberrations are required. Due to the point scanning nature of the AOSLO recordings, individual frames can be broken up into strips that record eye motion over time. Each of those strips are then cross correlated to a reference frame in real time, and the shift between the strip and the reference frame is the corresponding eye motion. This eye motion is then fed into an acousto-optic modulator (AOM), which acts as an optical switch to only allow the stimulation to be delivered at certain times, which correspond to positions in the scan (Arathorn et al., 2007). With this method, targeted stimuli can be delivered on the retina with a standard deviation of 0.32 arcmin (W. M. Harmening et al., 2014; Tuten et al., 2012).

The AOSLO stimulates at a different wavelength than that used for imaging, which can be shifted from each other both longitudinally (LCA) and transversely (TCA). To accommodate for LCA, the vergence of the light sources is adjusted to focus both at the same plane. Dispersion in the ocular media will cause light to deviate transversely by a magnitude exceeding the size of a single cone (Atchison and Smith, 2005). By collecting independent images in the imaging and stimulation channels, the relative shift in the two beams can be computed by cross-correlating the overlapped images. Compensation for TCA is done by setting the timings of the deliveries in the AOM to accommodate for the offset (W. M. Harmening et al., 2014).

1.2.3 Outer Retinal Degeneration Imaging and Clinical Functional Measures

Outer retinal diseases are characterized by the damage to photoreceptor structures, underlying RPE, or choroidal blood flow, and can cause vision loss and even blindness. Within outer retinal diseases, there are two subsets: inherited retinal diseases caused by mutations that miscode important proteins, and acquired degenerations such as age-related macular degeneration,

diabetic retinopathy, retinal detachment, and congenital eye diseases. Inherited outer retinal eye disease is further broken down by which photoreceptors are affected first: rods for rod-cone degeneration or cones for cone-rod dystrophy. Rod-cone degeneration (RCD), or most commonly retinitis pigmentosa, initially causes loss of peripheral vision and night vision (Hartong et al., 2006), while cone-rod dystrophy (CRD) produces loss of visual acuity, central vision, and color vision (Hamel, 2007).

The slow progressive nature of RCD makes it challenging to reliably monitor changes during a period of one or two years. In RCD, night vision and peripheral vision are lost earliest, but visual acuity can remain stable and normal until advanced stages of disease (Hartong et al., 2006). A longitudinal study of patients with retinitis pigmentosa (RP) followed for nine years found that visual acuity had the slowest decline relative to other measures such as visual field area and focal electroretinogram (ERG) (Holopigian et al., 1996). In addition, foveal measures of visual function demonstrate increased variability as retinal degeneration progresses (Bittner et al., 2011). Robust, sensitive measures of foveal health and cone loss, particularly ones that rely on structural measures rather than subjective psychophysical measures described above, could facilitate measurement of disease progression in patients with RCD.

Objective measures of retinal structure have become widely used because of advances in non-invasive, high-resolution imaging modalities that can be used to monitor changes in retinal and foveal topography. Spectral-domain OCT (SD-OCT), for example, provides non-invasive cross-sectional measures of retinal structures including photoreceptors (Birch et al., 2013; Hood et al., 2009). SD-OCT measures of outer retinal thickness have been shown to correlate with visual field sensitivity in eyes with RP (Hood et al., 2011; Smith et al., 2016), and may provide a useful, objective outcome measure for clinical trials (Birch et al., 2013; Hariri et al., 2016). Adaptive optics scanning laser ophthalmoscopy (AOSLO) allows for *en face* visualization of cone mosaics and measurements of cone spacing and density in normal and diseased eyes (Duncan et al., 2007; Roorda & Duncan, 2015; Talcott et al., 2011). Modern AOSLO systems are capable of imaging the cone mosaic at the fovea and yield measures of cone spacing (Foote et al., 2018; Merino et al., 2011; Pircher et al., 2008; Ratnam et al., 2013; E. A. Rossi et al., 2011; Wilk et al., 2017; T. Zhang et al., 2015) that are comparable to histological studies(Curcio et al., 1990).

Objective, structural measures of cone spacing may be more reliable than functional measures, but they are meaningful for patients only if visual function correlates with retinal structure. In cross-sectional studies of RCD patients, increases in cone spacing at or near the fovea were shown to correlate with visual acuity declines in a nonlinear way (Foote et al., 2018; Ratnam et al., 2013). Visual acuity decreased below 20/25 only in patients whose foveal cone density was 40-60% lower than normal, suggesting that visual acuity is preserved despite significant cone loss and is not a sensitive measure of foveal cone integrity (Foote et al., 2018; Ratnam et al., 2013). One limitation of prior cross-sectional studies, however, is that we could not know the extent to which the low cone densities resulted from actual cone loss or simply reflected the lower end of the spectrum of normal variation in cone density.

To understand how acuity changes during degeneration it would be desirable to track photoreceptor structure and function over time in the same RCD patients. Intervisit and interobserver variability in cone spacing measures from AOSLO images have been quantified in normal eyes and eyes with RCD; cone changes measured over time that are greater than baseline

intervisit and interobserver variability are likely to represent disease progression in RCD patients (Zayit-Soudry et al., 2015). In a retrospective study briefly summarized below, we compared foveal cone spacing with best-corrected visual acuity (BCVA) in patients with RCD and normal subjects, monitored longitudinally during periods ranging from 10 months to 5 years, to characterize changes in foveal structure and function during disease progression in eyes with RCD (Bensinger et al., 2019).

This retrospective study showed that cone spacing is correlated with visual acuity in normal subjects and RCD patients. However, as cone spacing increased in RCD patients over time, visual acuity did not concurrently change to reflect the progression of disease. Examples of cone spacing measurements change over time are shown in Figure 1.3. Likewise, OS+ thickness did not change over time in RCD patients with increased cone spacing, suggesting that cone spacing Z-scores may be a more sensitive measure of cone loss at the fovea than measures of visual acuity or OS+ thickness in patients with RCD.

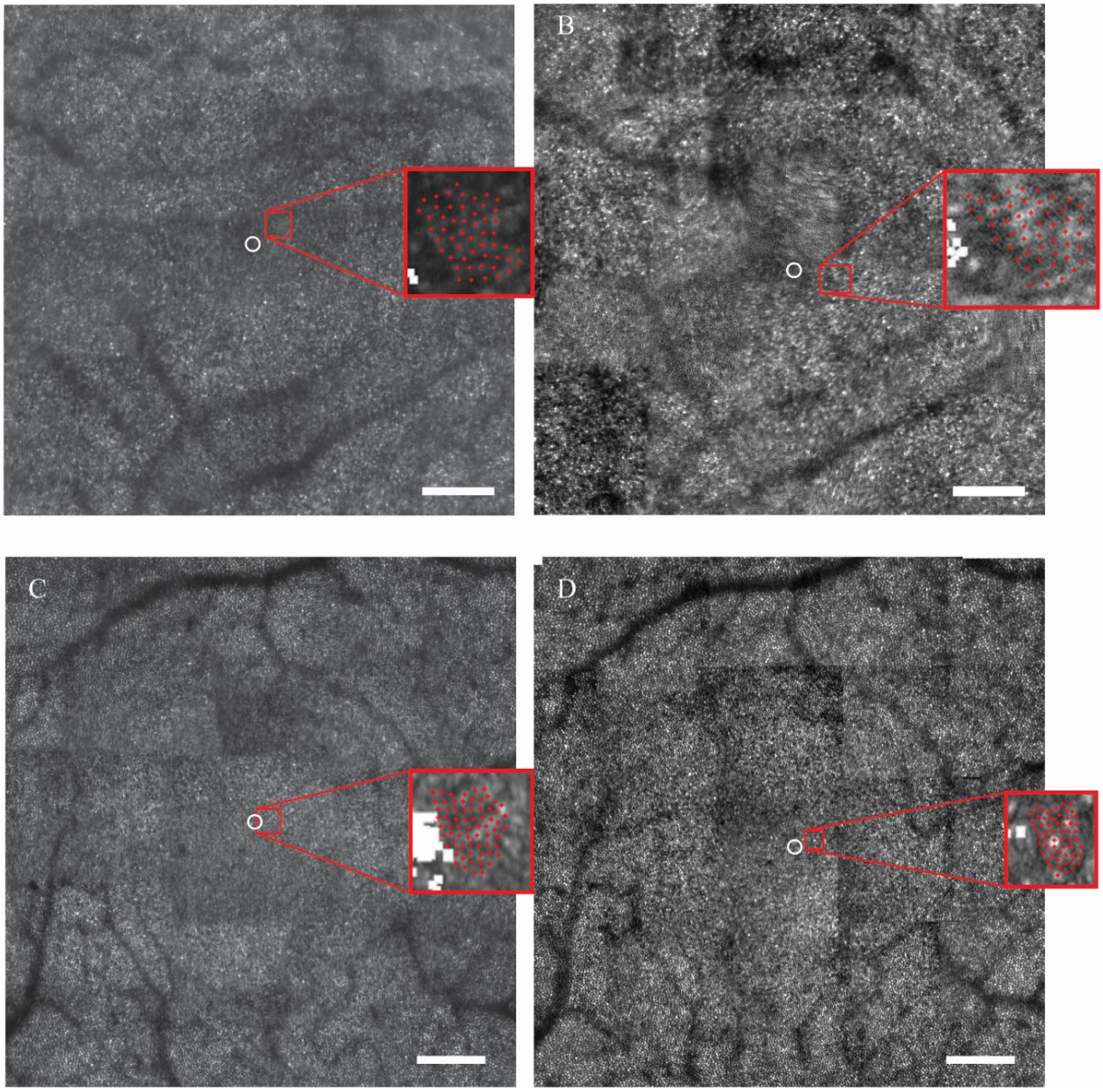

Figure 1.3 AOSLO Images of foveal mosaic for IRD patient and normal subject at two time points separated by one year. Baseline images are shown on the left two panels, and follow-up image are shown on the right. Scale bar 0.5 degrees. The PRL is indicated by the white circle. Insets to the right of each image show the cone locations used to compute cone spacing (red crosses).

1.2.3.2 Comparing AOSLO Metrics to Clinical Testing

This retrospective study is the first to assess longitudinal changes in foveal cone spacing in patients with RCD and normal eyes followed for at least 10 months, and to relate changes in cone spacing to clinical measures of foveal function and outer retinal thickness. The results represent an important continuation of a prior cross-sectional study in RCD patients that identified a significant, non-linear correlation between foveal cone spacing and function (Ratnam et al., 2013). Over the course of the longitudinal study, there was no measurable change in visual function (VA and foveal sensitivity), yet a small but significant amount of cone loss was detected. The increase in cone spacing in RCD patients is consistent with prior reports (Talcott et al., 2011). It was also confirmed that cone spacing Z-score was correlated with measures of visual function at the fovea (Ratnam et al., 2013).

This study further expanded the investigation of structural tests by including OCT. A significant negative correlation between cone spacing Z-score and OS+ thickness at the PRL, where cone spacing increased as OS+ thickness decreased, was found in normal subjects for both visits, but not at baseline or follow up visit for RCD patients. OS+ thickness was also compared to functional measures but was not significantly correlated with ETDRS letters read or with foveal sensitivity. In contrast, AOSLO-derived cone spacing Z-scores showed correlation with both visual acuity and foveal sensitivity.

Prior studies have suggested that the relationship between foveal structural measures and psychophysical measures is not linear (Geller et al., 1992; Ratnam et al., 2013). Using a theory that establishes resolvability as a measure directly proportional to the distance between foveal cones with intact connections to higher visual centers, 20/20 vision can be present with loss of 40% of foveal cones, 20/50 vision is expected with 10% of normal foveal cones and 20/200 is expected with 1% of normal foveal cones (Geller et al., 1992). Recent studies have used AOSLO to measure cone spacing near the fovea in eyes with retinal degeneration and have demonstrated that roughly 50% of cones can be lost before visual acuity declines below 20/25 (Foote et al., 2018; Ratnam et al., 2013). Because clinical visual acuity can remain normal as foveal cone spacing increases, there is likely to be redundancy in foveal cones for high contrast and fine detail visual acuity tasks. These results provide in vivo, longitudinal data to support predictions that cone density can decrease significantly before it manifests as a measurable decrease in visual acuity.

1.3 Previous Findings of Dysflective Cones

1.3.1 Normal Reflectivity Changes and Function

Cone reflectivity measured in the confocal AOSLO can vary significantly throughout the day and day to day(Pallikaris et al., 2003). Individual hyporeflective cones that are consistently hyporeflective throughout the day have shown normal visual function as shown in Figure 1.4 (Bruce et al., 2015). Intra-cone reflectivity changes over time could be due to outer segment length changes due to disc shedding (Anderson et al., 1980), and optical waveguiding (Marcos et

al., 1998). The cone inner segment is continuously renewing the outer segment's light sensitive discs and older discs are pushed down and undergo phagocytosis. Depending on where the cone is in this cycle could change the reflectivity of the cone. For the cone to properly waveguide light coming in from the pupil it has to be oriented toward the pupil, otherwise according to the Stiles Crawford effect the cone will not be reflective (Enoch & Birch, 1980; Westheimer, 2008).

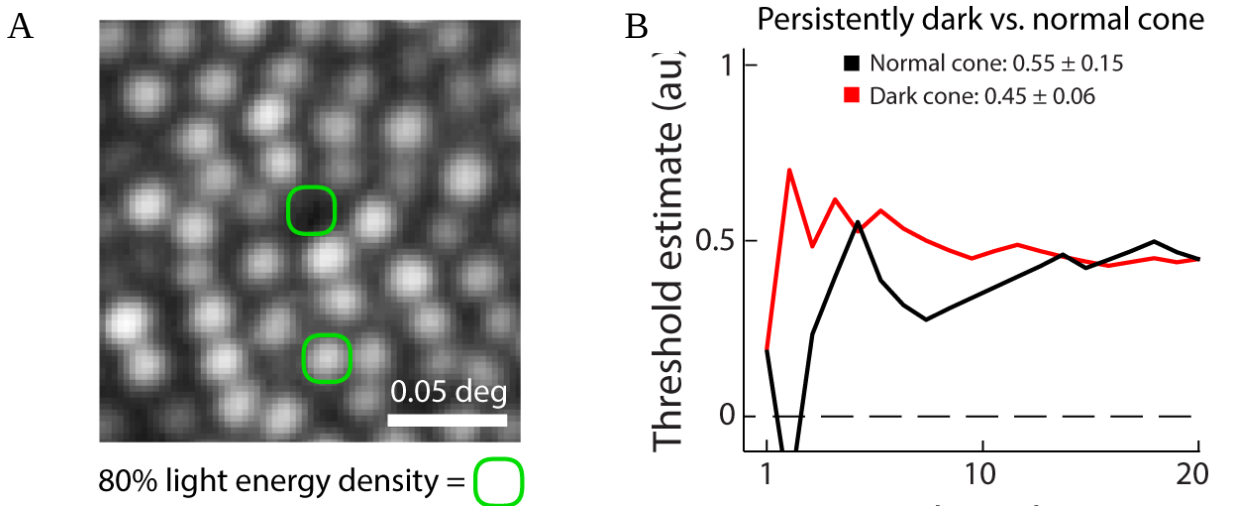

Figure 1.4 Confocal AOSLO images of cones with different reflectivity shown in A. Thresholds from adaptive optics microperimetry are shown in B with no significant difference between the two (*P*=0.49).

1.3.2 Previous Findings of Dysflective Cones and Potential Dysflective Cones in Retinal Disease

Dysflective cones are cones that do not reflect light normally, but still retain measurable function. This was defined through a study of a patient with acute bilateral foveolitis found to have measurable sensitivity and visual acuity within a retinal region that had no apparent cones in the confocal AOSLO image or in a spectral domain OCT image, a phenomenon that was termed dysflective cones (Tu et al., 2017). In the case reported by Tu et al. 2017, the dysflective cones appeared dark in confocal AOSLO images. In optical coherence tomography (OCT) the region of the B-Scan normally occupied by reflective layers corresponding to the inner-outer segment (IS/OS) junction and the cone outer-segment tips was transparent, although there was an intact external limiting membrane (ELM) as shown in Figure 1.5.

Similarly, cones in a dysflective state were observed in two patients with macular telangiectasia (Q. Wang et al., 2015). Interestingly, Wang et al found that regions where cones appeared to be absent in one visit recovered normal reflective properties in a subsequent visit as shown in Figure 1.6.

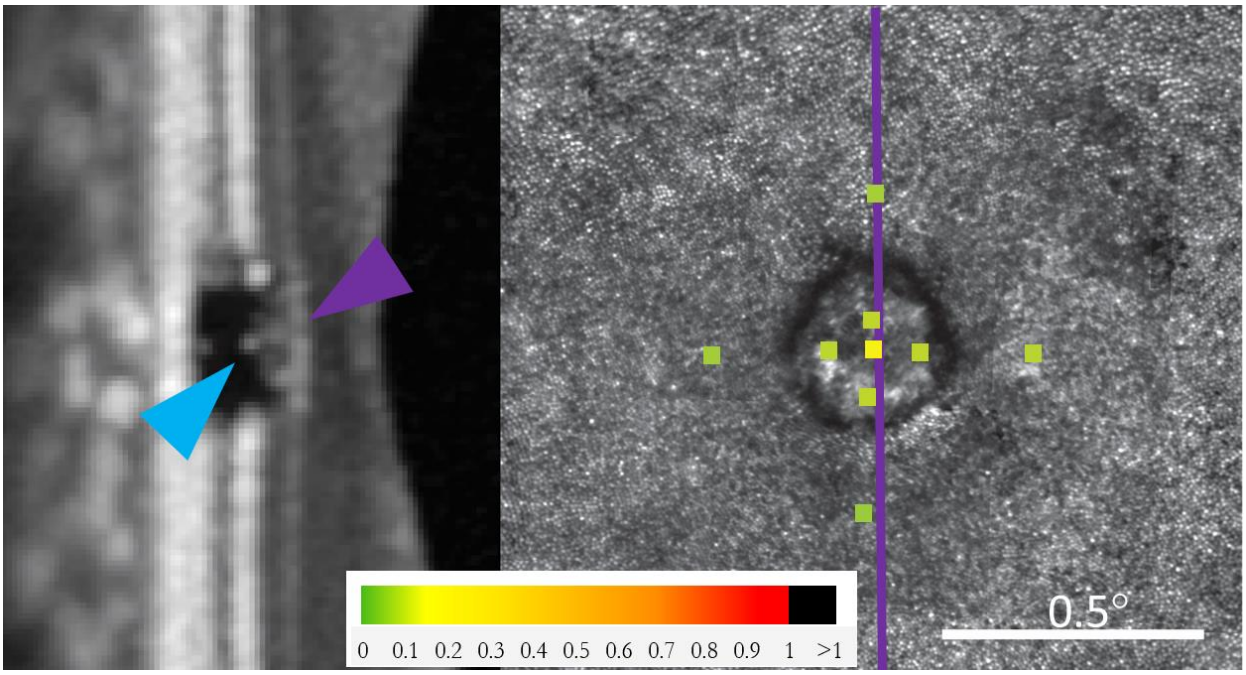

Figure 1.5 AOSLO confocal images of bilateral foveolitis shown on the right with AOMP testing shown by the colored boxes corresponding the color bar at the bottom. Purple line indicates the position of the OCT b-scan on the left with the purple arrow showing the intact external limiting membrane and the blue arrow showing the IS/OS junction break.

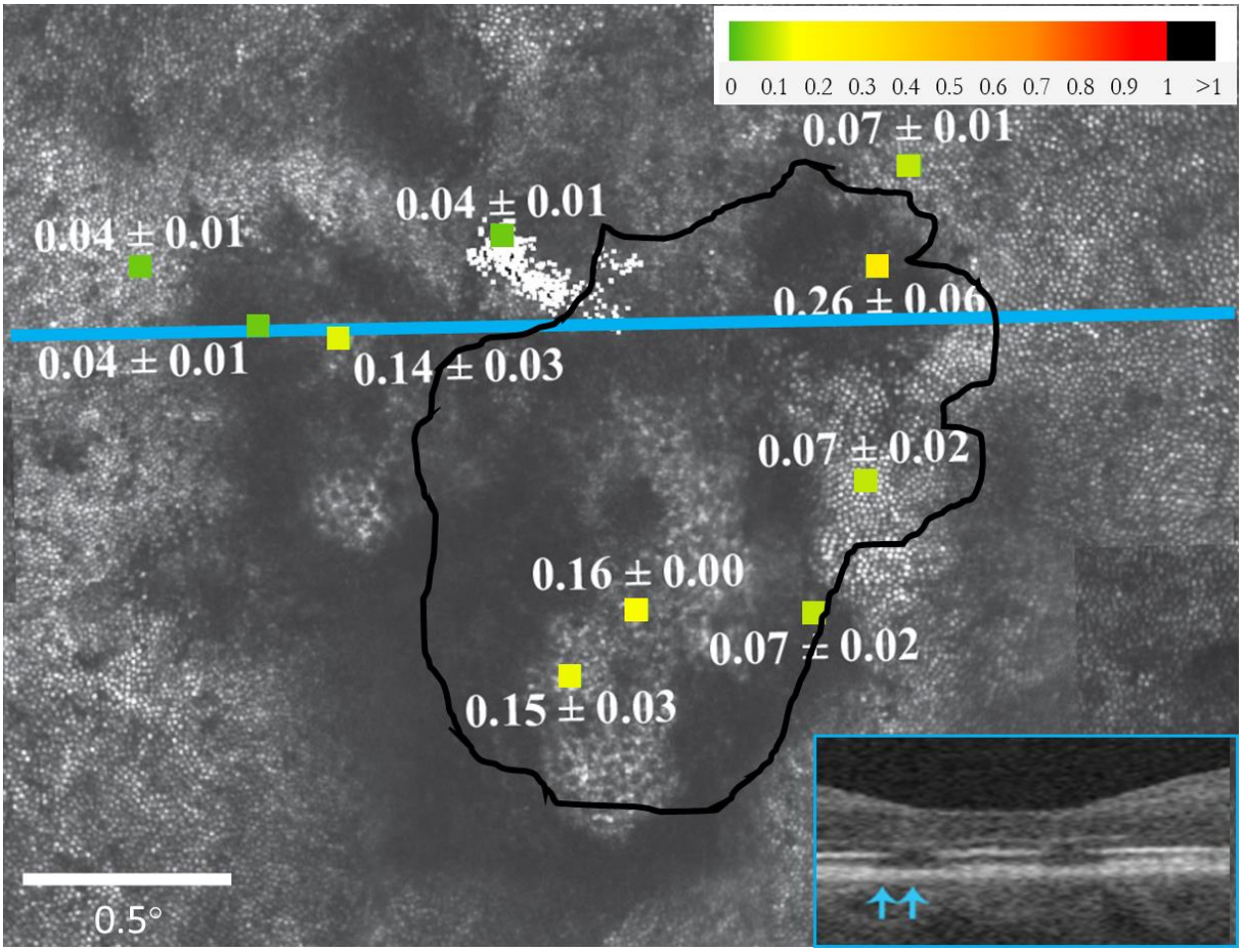

Figure 1.6 Macular Telelangectasia (MacTel) lesion confocal AOSLO images with AOMP measurements shown by the colored boxes corresponding the color bar at the top right. The black outline indicates the border of the lesion from 2 years earlier, showing that some areas recovered reflectivity over time. The blue line indicates the position of the SDOCT b-scan shown at the bottom right, with the arrows indicating the positions of the two testing locations along the b-scan. The PRL is indicated by the while dots. Adapted from Wang et al. 2015.

The recovery of reflective properties in cones of patients with macular telangiectasia has also been confirmed in 8 subjects using both confocal and split detector AOSLO imaging (Litts et al., 2020). Litts et al. discovered that cones not visible in confocal AOSLO images do appear using split-detector AOSLO imaging as shown in Figure 1.7. However, Litts et al. had no functional measures to determine whether these are dysflective cones, but the presence of inner segments is a likely indicator of function.

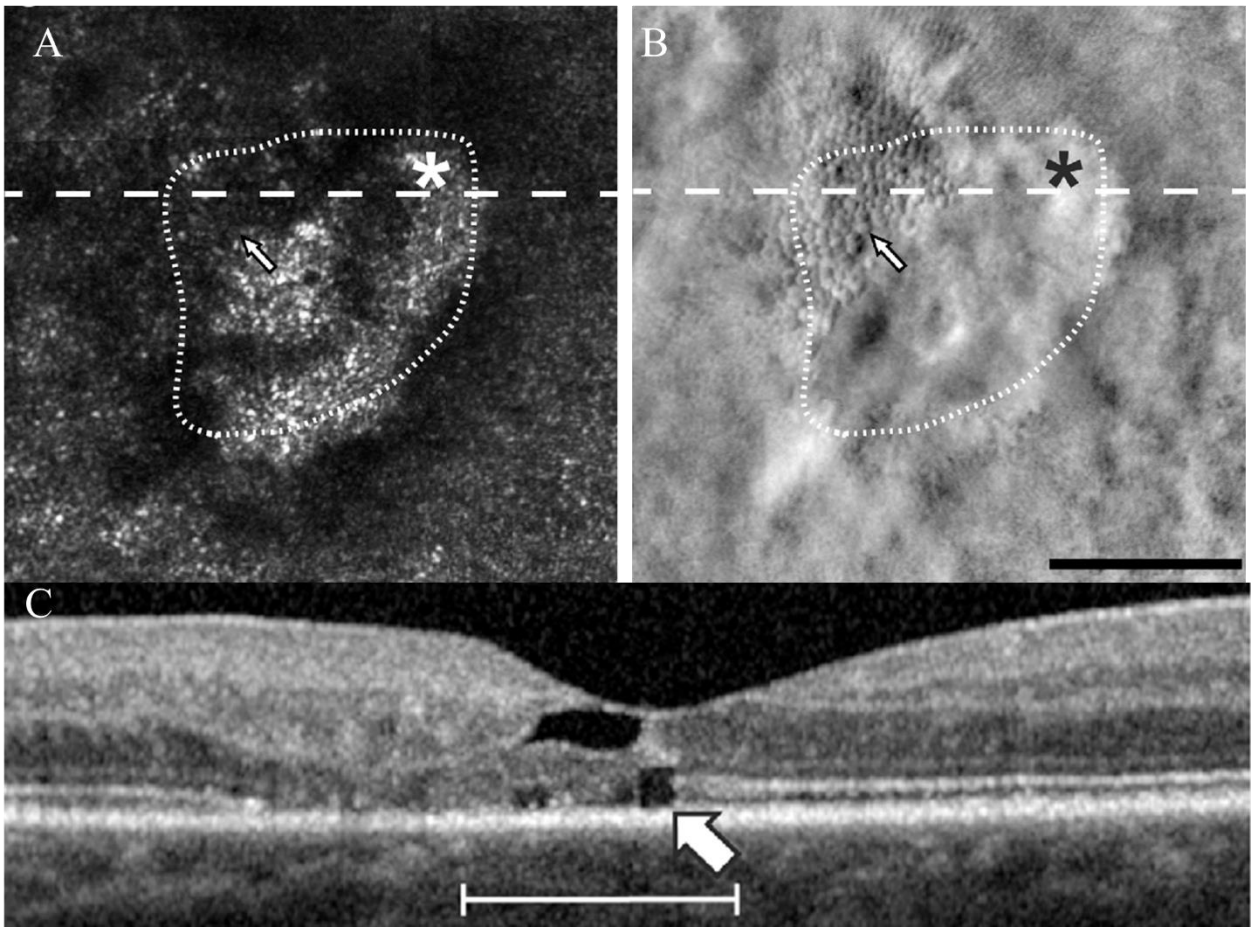

Figure 1.7 Adaptive optics confocal imaging (A) and split detector imaging (B) of remnant cones within a MacTel lesion. The dashed horizontal line indicates the location of the SDOCT b-scan shown in C. Remnant cone structure (white arrows) within or on the borders of the EZ lesions by split detector AOSLO (dotted outlines show approximate extent of lesion). The white line on SDOCT corresponds with the lateral extent of the AOSLO images. Asterisks indicates the location of the foveal center. Scale bar 100 µm (0.33º). Adapted from Litts et al. 2020.

1.3.3 Sources of Structural Change Affect Reflectivity but Not Function

The dysflective cones seen in patients in section 1.3.2 are significantly different from the normal day to day reflectivity variations as shown in section 1.3.1. What is unknown is the structural source of the lack of reflectivity in confocal images in the dysflective cones. Modeling of the sources of reflectivity of confocal AOSLO images shows that for the cone to be reflective, it requires the presence of at least one of the two strong refractive interfaces: the ellipsoid zone or IS/OS junction and the cone outer segment tip (COST) junction, with the apical processes of the retinal pigment epithelium (Meadway & Sincich, 2019). If both of those become disturbed the cone will appear dark in the confocal image.

It is important to begin to understand what the structures that affect the reflectivity of cones in AOSLO confocal images look like in histology. Nork et al. 2012 looked at macaque retinas following retinal detachment surgery, where a subretinal injection detaches the retina. The study used multifocal electroretinography (ERG) to show preserved function within the reattached area

despite a lack of reflectivity in the IS/OS band of an SD-OCT scan as shown in Figure 1.8A and B. Histology of the cone outer segment shows that the discs with cone photopigments are disrupted with large intradiscal spaces seen throughout the outer segment stacks in the areas of the former subretinal blebs. Histology of the RPE also show irregularity in the distribution of the pigment granules within areas with no pigment granules and some with pigment clumping. Taken together, it could be inferred that the intradiscal spacing is disrupting the refractive index difference that causes the IS/OS junction reflection and the areas with a lack of RPE pigment could be preventing COST RPE junction reflections.

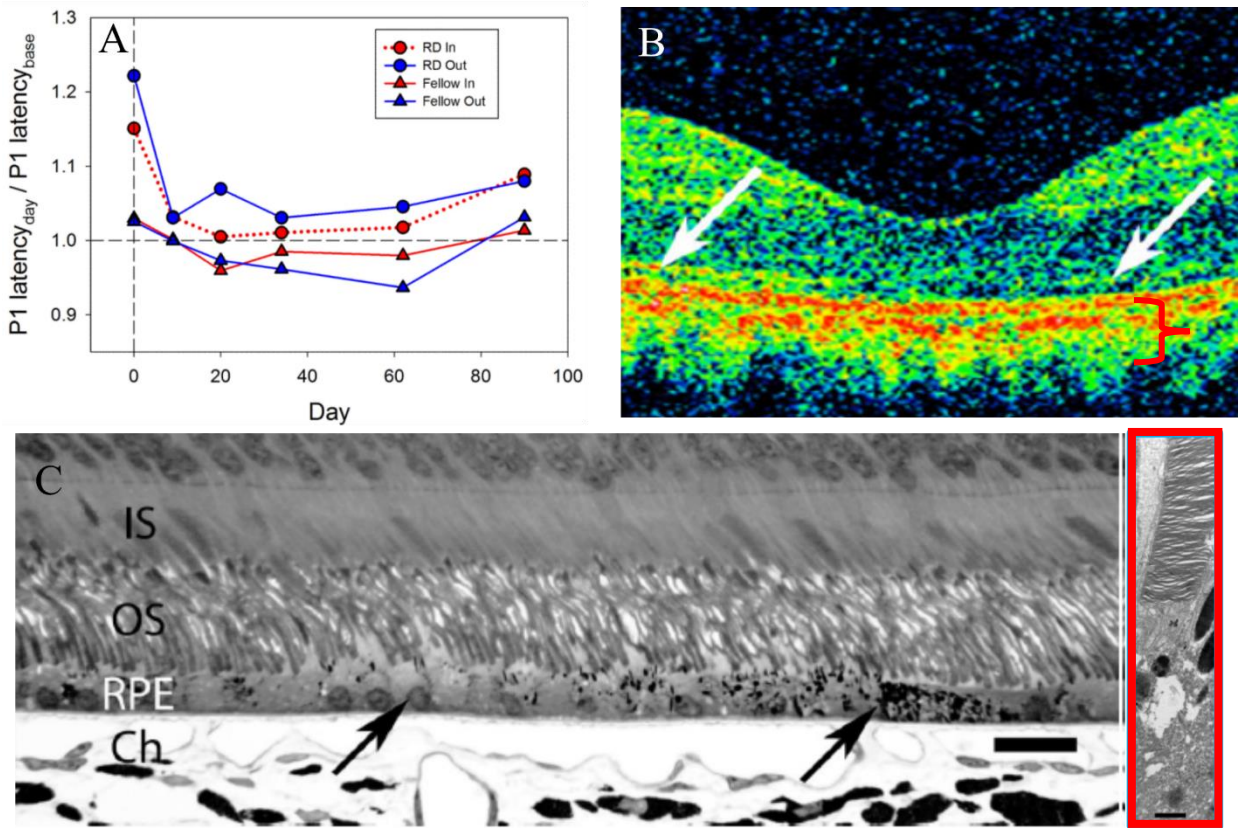

Figure 1.8 Dysflective Cones in macaque eyes 3 months after retinal detachment repair from a subretinal bleb. Panel A shows multifocal ERG results from the RD and the fellow eye. Panel B shows the OCT scan 3 months after RD with white arrows indicating the IS/OS junction. Panel C shows the histological cross section where the left black arrow indicates areas with a scarcity of RPE pigment granules and right black arrow indicates areas of pigment clumping. Blue bracket in panel B indicates the layers shown in the blue outlined image. Adapted from Nork et al 2012.

Chapter 2 | Dysflective Cones in Healthy Subjects

2.1 Abstract

Small patches of hyporeflective cone clusters are commonly found in the AOSLO images of normal healthy individuals. AOSLO and AOMP were used to assess the structure and function of hyporeflective areas in 3 healthy subjects and determined that these were in fact dysflective cones, i.e. hyporeflective cone clusters with intact function. Two of the 3 healthy subjects showed no difference in function in the dysflective area compared to adjacent areas, with one subject showing a 3x reduction in the sensitivity in the area of interest. Participants were monitored longitudinally and in many cases the hyporeflective areas recovered normal reflectivity and new hyporeflective spots were found in other areas of the retina.

2.2 Introduction

Cone photoreceptors initiate human photopic vision, providing the critical first response to light. Their tiled and close-packed arrangement within the retina limit, in part, the spatial resolution of the eye. Due to their high metabolic demand, cones are very susceptible to disease. Visualizing cone structure in living eyes offers a way to detect and monitor retinal disease. The adaptive optics scanning laser ophthalmoscope (AOSLO) system uses adaptive optics to correct for optical aberrations in the eye and achieve diffraction limited imaging of the individual photoreceptors at their smallest packing in the fovea (Liang et al., 1997; Roorda et al., 2002; Y. Wang et al., 2019). This high-resolution retinal imaging capability can be used to assess the health of cone photoreceptors by measuring the cones' intrinsic ability to reflect light with confocal AOSLO systems.

Cone reflectivity measured in the confocal AOSLO can be a challenging metric for retinal health due to significant spatial and temporal variations (Pallikaris et al., 2003). Intra-cone reflectivity changes over time could be due to a multitude of factors; light interference effects (Meadway et al., 2020; Putnam et al., 2010), outer segment length changes due to disc shedding (Anderson et al., 1980), pigment density changes (Masella et al., 2014), and optical waveguiding (Marcos et al., 1998). Inter-cone differences in reflectivity, however, are unrelated to cone type except under carefully controlled conditions (Roorda & Williams, 1999), and local reflectance angle differences are unlikely causes for large reflectivity differences (Roorda & Williams, 2002). Additionally, cone reflectivity has not been found to be related to the reflectivity of surrounding cones, and individual hyporeflective cones have shown normal visual function (Bruce et al., 2015).

Despite the sources of cone reflectivity variability described above, it is generally the case that regions in AOSLO and OCT images that exhibit a lack of normal reflections from the photoreceptors correspond to regions that lack functional cones. Multiple publications confirm this for many different diseases including retinitis pigmentosa (Duncan et al., 2007; Sun et al., 2016), choroideremia (Morgan et al., 2014; Syed et al., 2013), cone-rod dystrophy (Song et al., 2018; Wolfing et al., 2006), age-related macular degeneration (Zayit-Soudry et al., 2013), and Stargardts disease (Chen et al., 2010; Song et al., 2015).

However, the absence of visible cones in a retinal image, even over large areas, does not necessarily mean that cones are not present or that they are not functional. A study of a patient with acute bilateral foveolitis found measurable sensitivity and visual acuity within a retinal region that had no apparent cones in the confocal AOSLO image or in a spectral domain OCT image, a phenomenon that was first termed by Tu et al to be *dysflective cones* (Tu et al., 2017). Dysflective cones are defined as cones that do not reflect normally, but still retain measurable function. In the case of Tu et al, the dysflective cones appeared dark in confocal AOSLO images and, in optical coherence tomography (OCT) images, the region of the B-scan normally occupied by reflective layers corresponding to the inner-outer segment (IS/OS) junction and the cone outer-segment tips were transparent, although there was an intact external limiting membrane (ELM). Similarly, cones in a dysflective state were observed by Wang et al in two patients with macular telangiectasia (Q. Wang et al., 2015)

Importantly, Wang et al found that regions where cones appeared to be absent in one visit recovered normal reflective properties in a subsequent visit (Q. Wang et al., 2015). The recovery of reflective properties in cones of patients with macular telangiectasia has also been confirmed in a more recent and extensive study that employed both confocal and split-detector AOSLO imaging (Litts et al., 2020). Similar recovery has also been observed in OCT images in patients following macular hole repair (Landa et al., 2012; Randerson et al., 2015). Neither of the latter three reports, however, were able to directly test the function of the purported dysflective cones. Litts et al. (Litts et al., 2020) also discovered that although cones may not appear in confocal AOSLO or OCT images, the inner segments of the cones *do* appear using split-detector AOSLO imaging. Unlike AOSLO and OCT, both of which employ confocal imaging, split-detector AOSLO is a form of phase-contrast imaging and does not rely on direct back-scattering for detection and resolution of cell structure (Guevara-Torres et al., 2020; Scoles et al., 2014).

When imaging healthy eyes in the AOSLO, in addition to the normal cone-to-cone variability, we frequently observe small hyporeflective patches in the cone mosaic. These hyporeflective patches have a similar appearance to clusters of dysflective cones seen in patients and are also transient, both appearing and recovering normal reflectivity similar to dysflective cones in MacTel patients (Bensinger et al., 2018; Q. Wang et al., 2015). Thus, we were motivated by these observations to investigate the frequency of occurrence and timelines of hyporeflective patches in normal healthy eyes and to evaluate function within these patches. We hypothesize that these hyporeflective patches contain dysflective cones (ie they retain function). The AOSLO system used in this study has been equipped with real-time eye tracking and has the ability to deliver light to targeted retinal locations (Arathorn et al., 2007) and offers an unprecedented ability to test function in regions as small as a single cone (W. M. Harmening et al., 2014).

2.3 Methods

2.3.1 Human Subjects

The experiments were approved by the University of California, Berkeley Committee for the Protection of Human Subjects and research procedures followed the tenets of the Declaration of Helsinki. Informed written consent was obtained from all subjects after explanation of the nature and possible consequences of the study, including the possible use of their images and data for retrospective review and ancillary studies.

2.3.2 AOSLO Imaging

AOSLO images of the cone mosaic were acquired using a multiwavelength AOSLO platform, the details of which have been described previously (Grieve et al., 2006; W. M. Harmening et al., 2014; Mozaffari et al., 2020). In the system used for this study, the light source was a supercontinuum laser (SuperK EXTREME, NKT Photonics, Birkerod, Denmark) that was divided into multiple channels using a series of custom-built fiber couplers to provide an 840-nm channel for IR imaging, a 680-nm channel for visible red imaging, and a 543-nm channel for visible stimulation. The 543-nm stimulus delivery was chosen for functional testing since it was equally sensed by L and M cones. The system measured wave aberrations with a custom-built Shack Hartmann wavefront sensor and employed a deformable mirror with 97 actuators (DM97, ALPAO, Montbonnot-Saint-Martin, France) to compensate the aberrations.

2.3.3 Retrospective Survey of Healthy Hyporeflective Cones

Images previously collected using AOSLO systems were surveyed. The AOSLO raster was set to 0.9° × 0.9° (~270 × 270 microns) with an average sampling resolution of 9.48 pixels per arcminute. 10-second videos were recorded with 680-nm visible red light for the majority of imaging but some subjects were recorded at 840 nm. Videos were recorded at 9 locations at and around the fovea comprising a minimum 1.8° x 1.8° area. The survey included images from 74 eyes of 47 subjects (12 male, 25 female). The average age for these subjects was 28.4, maximum age of 52 and minimum age of 20. The primary purpose for imaging 62 of the eyes (84% of the study) were for a study on foveal cone spacing as a function of axial length (Y. Wang et al., 2019). The remaining 12 eyes were imaged for various other studies. In some cases, an image from a single video of a ~0.9° field centered on the fovea was used.

2.3.4 Tracking Hyporeflective Cone Progression

Suspected dysflective cones were identified as contiguous hyporeflective patches in the cone mosaic with no discernible cones. Patches of cones comprising as few as three hyporeflective cones were included in this report. In addition to the subjects used in the retrospective survey, 7 new subjects were recruited for imaging following the same imaging protocol as Wang et al. (Y. Wang et al., 2019).

Whenever possible, the subjects from both the retrospective study and newly recruited subjects with patches of suspected dysflective cones were brought back for follow up imaging. 2 subjects from the retrospective study already had follow-up imaging done, while 8 additional subjects were brought back specifically for the purposes this study.

2.3.5 Analyzing Hyporeflective Cones

The raw AOSLO videos collected in this survey were converted to high-resolution, high-signal-to-noise images first by correcting for eye movements offline using custom Matlab software and then adding all registered frames (Stevenson & Roorda, 2005). Briefly, the eye movement correction process involves breaking each frame of the 680-nm or 840-nm acquired video into strips and cross correlating them to a reference image. The reference image was created by cross correlating then summing multiple frames of the video together to obtain a large reference image with less eye-motion distortion than a single frame. For eyes with the 9 imaging locations comprising a 1.8° x 1.8° field each image was cropped and assembled to form a montage (Adobe

Photoshop, Adobe Inc, San Jose, USA) and the dysflective regions were identified in these montages.

Whenever suspected patches of dysflective cones were identified, images were histogram normalized to a reference image and the border of the hyporeflective region was calculated using the fast-marching method(Liao et al., 2013; Peng et al., 1999). The border was measured by selecting a pixel in the dysflective region to use as a reference intensity then computing the weight for each pixel in the image based on the difference between each pixel's grayscale intensity and the reference. The image was then segmented using the fast-marching method with a consistent threshold and the reference pixel as the seed location (Liao et al., 2013; Peng et al., 1999). Following that, any holes within the segmentation area were filled, and the perimeter of the segmented area was calculated.

2.3.6 Functional Testing

Adaptive optics microperimetry (AOMP) was used to assess the function of areas identified as possible dysflective cones in 4 healthy subjects. The AOSLO can test the function of the retina with cellular accuracy by measuring and correcting retinal image motion in real time and delivering an AO-corrected, stabilized stimulus directly to a targeted retinal location (Arathorn et al., 2007). Previous reports from our laboratory confirm that the AOSLO system can target individual cones and assess their sensitivity with AOMP (W. M. Harmening et al., 2014; Tuten et al., 2012).

In this study, AOMP thresholds were computed as the average of 2, 35-trial adaptive staircase (QUEST) sessions (Watson & Pelli, 1983). Adjacent normal-appearing mosaics of cones were used as a control. Due to the small size of the hyporeflective patches, AOMP utilized a stimulus size of less than 1 arcmin. Transverse chromatic aberration, due to the difference in imaging (840 nm) and testing (543 nm) wavelengths, was measured objectively before and after AOMP testing (Wolf M. Harmening et al., 2012). During the trials, a pupil camera was used to ensure the eye remained well-aligned in the system so that TCA would not change during the trials by more than 0.5 arcmin (Boehm et al., 2019). Each trial comprised a stimulus that was delivered over 6 frames (~150 msec). A 1-second AOSLO video, which contained a digital mark indicating the location of the stimulus on each frame, was recorded for each trial.

The exact location of the tested region for each threshold measurement is affected by several factors.

1. Due to real-time tracking errors, the stimulus was not delivered to the same exact location of the retina on each frame of each trial. All trials where the delivered stimulus in any one of the six frames was off by more than 20 pixels (~2 arcmin) were removed from the QUEST staircase. The remainder of the stimulus locations formed a tight scatter plot of tested locations about the targeted area.
2. After the AO-correction the focused point spread function (PSF) is still blurred by diffraction. We approximated the final PSF after correction to be a diffraction-limited Airy pattern.
3. The stimulus itself has a finite size that is set by the operator. In this experiment that stimulus was a square patch less than 1 minute of arc in size.

Considering the three factors described above, the accuracies of the targeted locations in a complete AOMP session were depicted by convolving the stimulus with the diffraction limited

Airy pattern and summing over the complete range of locations where the stimulus was delivered over all trials. A contour map was then generated to indicate the average distribution of light delivered to the retina on a normalized percentage scale.

Thresholds were computed on a normalized scale from 0 to 1, where 1 is the maximum amount of power that we could deliver in any session. For these particular measurements, a value of 1 corresponded to a maximum luminance of 38 cd/m^2. The background was dominated by the 840-nm imaging channel and when combined with the leak in the 543-nm stimulus channel our background was, on average, about 4 cd/m^2. At this light level rods should be saturated, and within the 1.8° field there should be few if any rods in the area (Aguilar & Stiles, 1971).

2.4 Results

2.4.1 Survey of AOSLO Images

In our retrospective study, confocal AOSLO images revealed patches of suspected dysflective cones in distinct areas in the foveal region in many of our subjects, none of whom had any known ocular pathology. We found that 19 out of the 47 individuals had one or more hyporeflective patches in one or both eyes. Example images of these hyporeflective patches are shown in Figure 2.1. The areas are generally close to circular, with an average circularity index (ratio of area to perimeter) of 0.73 with a standard deviation of 0.029 (Domalpally et al., 2013). The average area of the hyporeflective patches was 6.3 arcmin^2 (range 2.2 arcmin^2 to 57.3 arcmin^2).

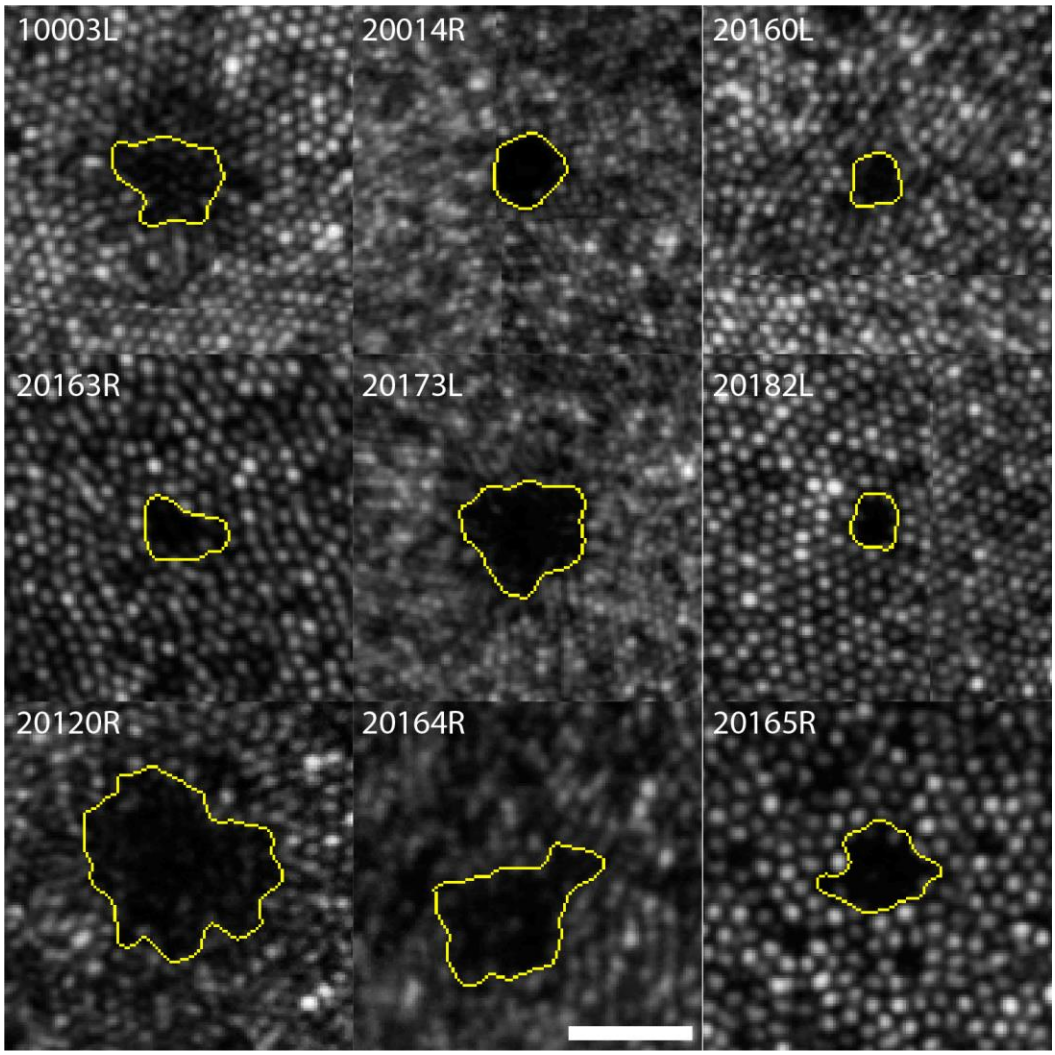

Figure 2.1 Hyporeflective cone clusters from 9 subjects. Yellow borders were created using the fast-marching method. Scale bar is 0.1 degrees and applies to all frames.

Whenever possible, images of the same region taken on different days were compared. Time spans for follow-up imaging ranged from 3 weeks to 1 year. The areas for the ten subjects with repeated imaging sessions are shown in Figure 2.2. Of the 14 hyporeflective patches in 10 of the subjects that were present at the first imaging session, 9 fully resolved at follow up, denoted by an **x** at the lower terminus of the timelines. We were unable to measure the exact time point when the hyporeflective patches appeared or resolved. New clusters spontaneously appeared in other retinal locations in two eyes from two subjects and are denoted by an **x** at baseline.

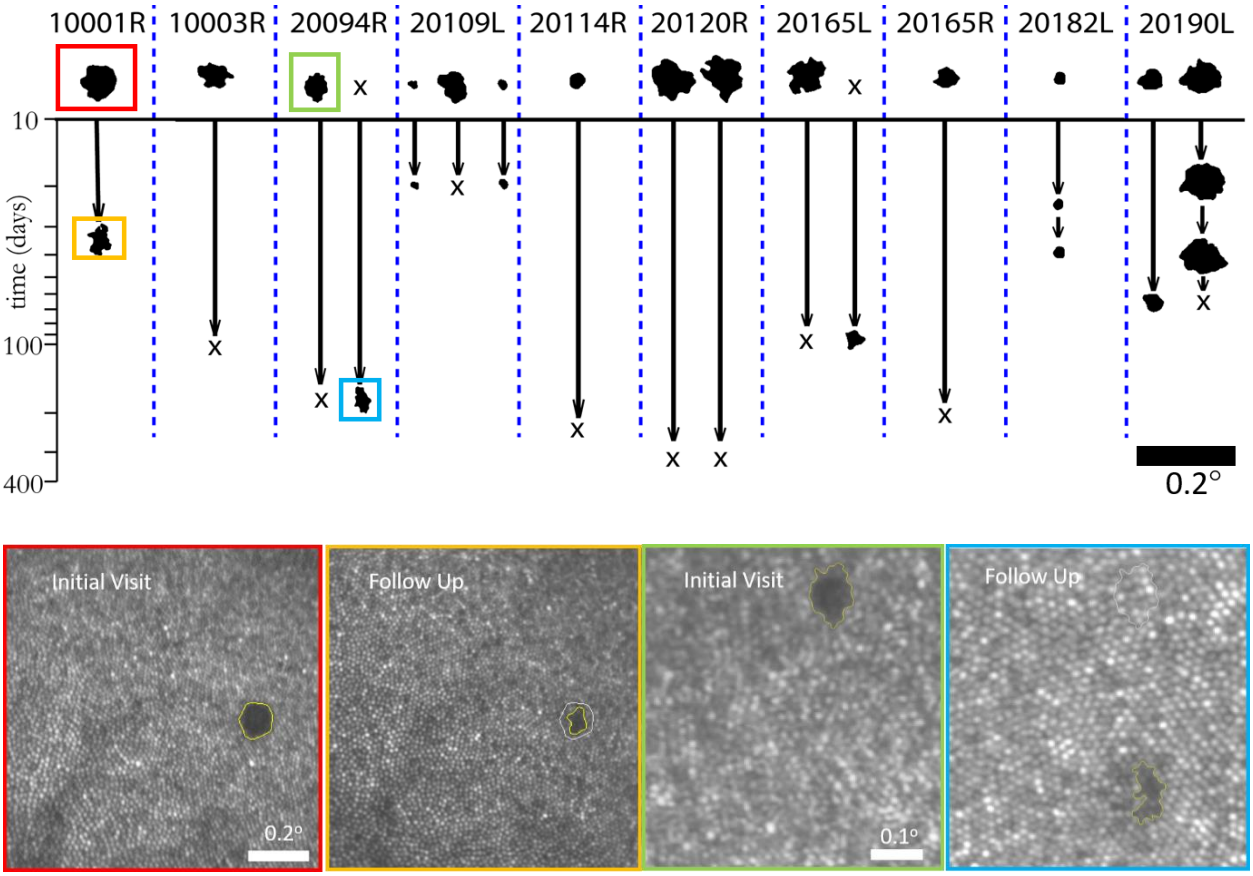

Figure 2.2 Timeline of hyporeflective patches in healthy eyes. The y axis is the time in days since their original sighting. An x at follow up indicates that the area resolved over time, and an x at the original imaging session indicates that a new hyporeflective patch was seen at follow up. The images corresponding to the patches inside the colored boxes are shown in the lower panels. Subject 10001R shows partial recovery of reflectivity over 5 weeks. Subject 20094R has complete recovery of one hyporeflective patch with a new hyporeflective patch appearing in a new location.

Areas that recover reflectivity were verified not to result from cones migrating to that space by performing a cone-to-cone match between the two visits. To illustrate this, Figure 2.3 shows examples from one subject where the initial cone locations surrounding the hyporeflective patch are shown in blue and the cone locations in the follow up visit are shown in orange.

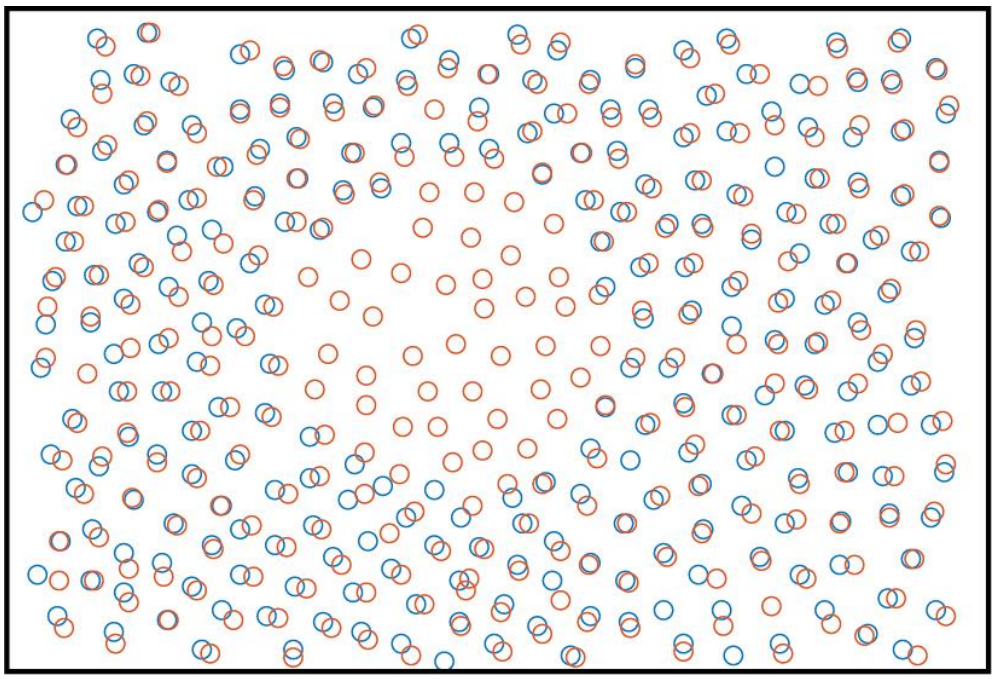

Figure 2.3 Cones do not migrate into the hyporeflective regions. Cone locations from subject 20190 from the initial visit are indicated by the blue circles. The initial selections surround the central hyporeflective patch where no cones were visible. The orange circles indicate the cone locations at follow up. There is a nearly perfect correspondence between the original and final cone locations. The only change is the new selections of the cones that regained their reflective properties at follow up.

2.4.2 Functional Testing

Light sensitivity thresholds within hyporeflective patches were measured in 4 subjects. All subjects had measurable sensitivity in their hyporeflective patches, thereby confirming our suspicion that they indeed contained dysflective cones. 3 of the 4 subjects showed no differences in sensitivity within their hyporeflective patches compared to adjacent areas although one subject 40104 had 3 times reduced sensitivity within their hyporeflective patch as shown in Figure 2.5 and Figure 2.5.

Cones within two of the four healthy subjects' hyporeflective patches regained normal reflective properties after 2-3 weeks as shown in Figure 2.5Figure 2.5. We had the opportunity to perform AOMP in one of the subjects (subject 20114, lower panels on Figure 2.5). The thresholds were similar before and after recovery of reflectivity.

The targeting accuracy for all subjects is indicated by contour plots on Figure 2.5 and Figure 2.5, computed as described in section 2.6. TCA was measured before and after each session and were confirmed to be within 0.55 arcminutes in both the x and y direction of each other for all subjects.

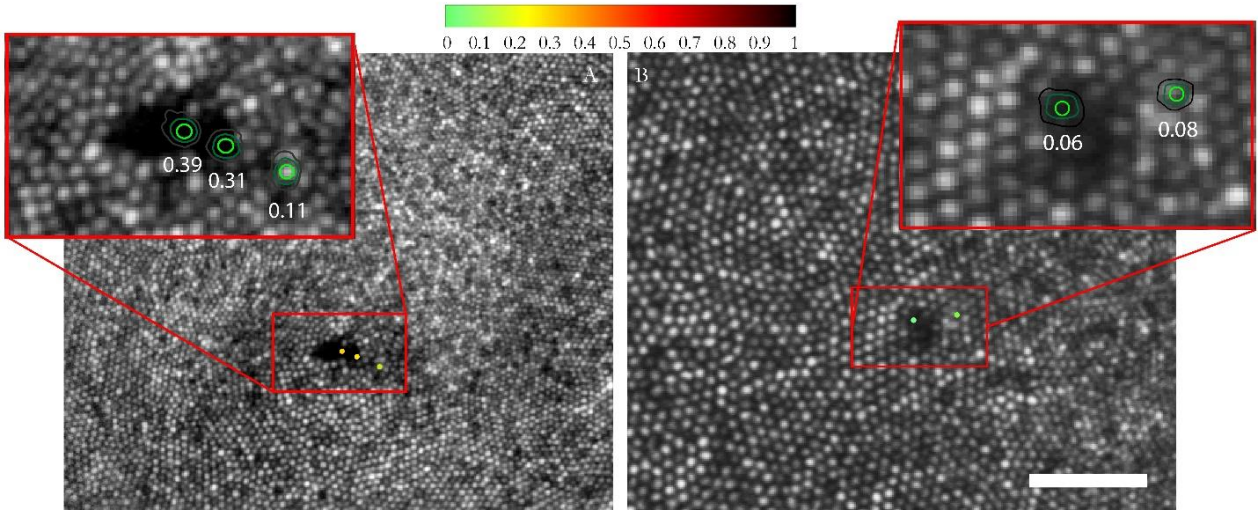

Figure 2.4 Microperimetry results for subjects 40104 (left) and 20182 (right). The tested locations are indicated by dots in the larger field image and by contours in each magnified inset where the color of the dot and the central contour depicts the threshold as indicated by the colorbar. Scale bar is 0.2 degrees.

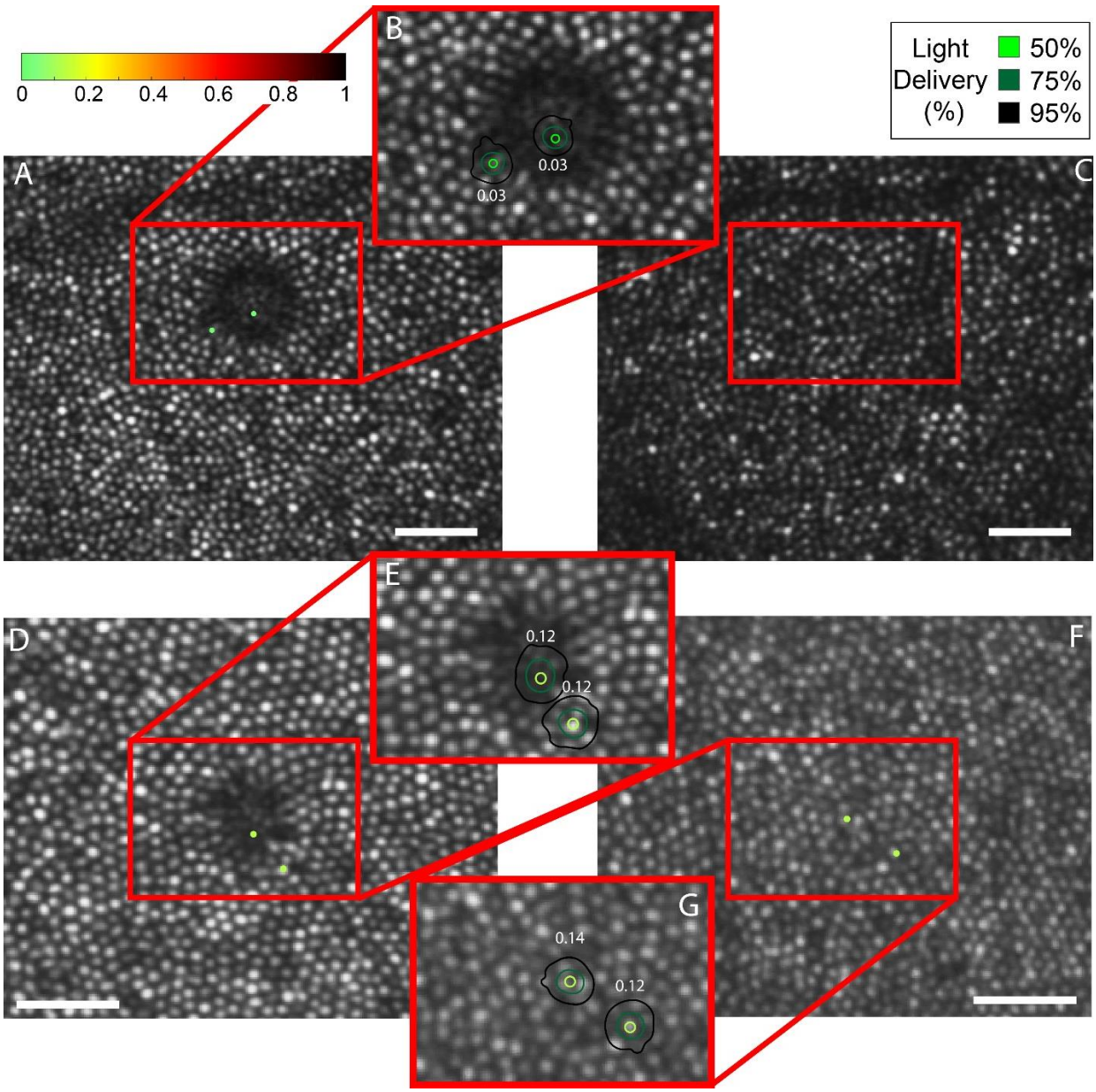

Figure 2.5 Microperimetry results for subject 20190 (top) and 20114 (bottom). The tested locations are indicated by dots in the larger field image and by contours in each magnified inset where the color of the dot and the central contour depicts the threshold as indicated by the colorbar. Panel C & F to the right show follow up AOSLO image (3 weeks for 20190 and 2 weeks for 20114) after the first microperimetry session where the dysflective cones have recovered their reflectivity. Here the red box indicates the same location as the red box in panel A & D. Panel F also shows the microperimetry results in the location with recovered reflectivity. Scale bar is 0.1 degrees.

2.5 Discussion

Patches of dysflective cones have been identified in healthy subjects for the first time. These areas show intact visual function despite reduced reflectivity. We also show that dysflective cone patches in healthy eyes are transient, both resolving and appearing in new locations. We found

that dysflective cones in normal eyes have similar or slightly reduced function compared to the surrounding cones.

2.5.1 The Causes for Dysflective Cones Remain Unknown

The reason why cones go into and recover from a dysflective state is yet unknown. Reflected light from cones in retinal images originate from two primary reflection sites within the cone: the inner-outer segment junction (IS/OS) and the cone outer segment tips (COST). These reflection sites are readily visible in OCT images, which visualize sources of reflection by their time of flight (Jonnal et al., 2014; F. Zhang et al., 2019). In an AOSLO, the two reflections combine and are visualized at the point where they emerge from the inner segments near the external limiting membrane (Meadway & Sincich, 2018; Putnam et al., 2010). Since the two sources of light combine in an AOSLO, there is a possibility that the cone reflectivity reduces because of destructive interference between the two sources within the waveguiding cones (Meadway & Sincich, 2018, 2019; Putnam et al., 2010). There are two reasons why interference is an unlikely cause for cones to be in a dysflective state. First the hyporeflective patches persist for time, whereas interference effects tend to change rapidly (Cooper et al., 2018; Jonnal et al., 2007). Second, the short coherence length typically used in an AOSLO minimize the amount of interference that can occur (Meadway & Sincich, 2019; Putnam et al., 2010). Ruling out interference, then it must be the case that both sources of reflection within a dysflective cone are diminished. This is indeed observed in OCT images (Tu et al., 2017; Q. Wang et al., 2015). A structural change in the outer segment is likely to be the cause for this. The persistence of light sensitivity, however, implies that phototransduction is still occurring.

Unfortunately, alternate imaging methods were not able to provide additional structural details of these dysflective cones. Commercially available SD-OCT systems did not offer the sampling density or resolution to resolve these hyporeflective patches, as it was unclear which layer the reduced reflectivity was within the outer retina. We also attempted to visualize the cone inner segments using split-detection AOSLO (Scoles et al., 2014), which is a form of phase-contrast imaging that reveals cells by their refractive state rather than their reflective properties. However, split-detector has inherently poorer resolution than confocal imaging, and the cone inner segments near the fovea in our subjects were too small to resolve using that modality. Notably, other studies have used split-detector to visualize inner segments in non-reflective cones away from the foveal center (Langlo et al., 2016; Litts et al., 2020; Scoles et al., 2014; Sun et al., 2016). Given that we measured function even in regions where we failed to see evidence of photoreceptor cells, and that in many instances we observed a full recovery of reflectivity, it is highly likely that these dysflective areas contained a complete mosaic of cone photoreceptor inner segments.

2.5.2 Comparison with Previous Reports

The current results are consistent with a report from Bruce et al. who found normal function in individual weakly reflective photoreceptors (Bruce et al., 2015). In that study, individual photoreceptors were tracked in an AOSLO, and some were found to have intermittent recovery of reflectivity while others remained persistently hyporeflective over as long as 672 days. The function of those individual weakly reflective photoreceptors was measured using a similar AOMP thresholding paradigm and the same 543-nm stimulating wavelength and it was found that both persistently hyporeflective cones and intermittently hyporeflective cones had no detectable difference in threshold from normal cones.

Despite the similar findings, the current study is distinct in that we chose to study hyporeflective patches with areas greater than 3 hyporeflective cones. Whereas the normal variations in reflectivity could arise from a multitude of factors, these normal variations do not explain the larger patches of hyporeflective cones that we observed over multiple imaging dates(Bruce et al., 2015; Meadway & Sincich, 2019; Pallikaris et al., 2003; Putnam et al., 2010).

The dysflective cones that we observe in normal eyes have a similar phenotype to those observed in clinical conditions including a case study in which dysflective cones were observed in a patient with acute bilateral foveolitis (Tu et al., 2017) and patients with Macular Telangiectasia that had dysflective cones that recovered reflectivity at the second time point (Q. Wang et al., 2015).

2.6 Conclusions

Small patches of dysflective cones are relatively common in the retinas of normal healthy individuals. These dysflective cones are not associated with any pathology, they exhibit normal or slightly reduced sensitivity and in many cases are transient, appearing and resolving over time.

Contents of this chapter have been submitted for publication: Bensinger, E, Wang, Y, Roorda AJ, Duncan JL. Dysflective Cones in Healthy Subjects

Chapter 3 | Dysflective Cones in Macular Telangiectasia

3.1 Abstract

AOSLO and AOMP were used to assess the structure and function of areas identified as possible dysflective cones in three MacTel patients. Subjects were imaged with confocal AOSLO, split detector AOSLO, and OCT, and when possible, follow up images were acquired one year later. Participants had reduced, but measurable, sensitivity within the dysflective area. One patient had no measurable sensitivity in the middle of the lesion, but measurable sensitivity at the dysflective border. These corresponded to regions in the split-detection images without and with visible inner segments, respectively. Split detector imaging further refined the dysflective cone phenotype in MacTel patients and suggests that visible inner segments are present in dysflective cones with measurable function.

3.2 Introduction

Macular telangiectasia type 2 (MacTel) is a bilateral progressive degenerative disorder characterized by loss of retinal transparency and macular luteal pigment, inner and outer retinal cavitations, telangiectatic retinal capillary abnormalities and discrete regions of photoreceptor loss associated with dense scotomas (Mukherjee et al., 2017; Sallo, Peto, Egan, Wolf-Schnurrbusch, Clemons, Gillies, Pauleikhoff, Rubin, Chew, & Bird, 2012). Studies of histological specimens have demonstrated primary loss of Muller cells, indicating that MacTel is a primary neuroglial disorder with secondary photoreceptor disruption and loss (Charbel Issa et al., 2013; Powner et al., 2013). Participants with MacTel have characteristic inner retinal cavitations and outer retinal lesions which appear on spectral domain optical coherence tomography (SD-OCT) imaging as a hyporeflective or disrupted reflections from the junction of the inner and outersegment (IS/OS) and from the cone outer segment tips (COST) (Clemons et al., 2010). The characteristic retinal vascular changes in eyes with MacTel occur secondary to Muller cell and photoreceptor loss (Powner et al., 2010, 2013). Disruptions to the IS/OS band in SD-OCT images correlate with photoreceptor dysfunction and vision loss (Mukherjee et al., 2017; Q. Wang et al., 2015).

However, recent studies have shown that remnant cone inner segment structure can be seen in some areas of MacTel lesions with adaptive optics scanning laser ophthalmoscope (AOSLO) split-detector imaging (Litts et al., 2020). Previous studies have also shown that within MacTel lesions where there are IS/OS disruptions and a lack of visible cones in confocal AOSLO images there is measurable, albeit reduced, visual function as measured using a technique called AO microperimetry (Q. Wang et al., 2015), (Tuten et al., 2012). Since then, a new term - *dysflective cones* - has been used to describe those cones that lack reflectivity in confocal AOSLO and OCT images but have measurable function. The term was first used to describe a participant with bilateral foveolitis and a lack of cone reflectivity but measurable function at the fovea (Tu et al., 2017). In the participant with bilateral foveolitis SD-OCT showed IS/OS disruption with an intact, but somewhat hyperreflective external limiting membrane band. Similar phenotypes in SD-OCT images have been reported for participants with MacTel (Q. Wang et al., 2015) and after macular hole repair (Landa et al., 2012), but previous studies have not evaluated the visual function of cones with visible inner segments in the presence of IS/OS disruption. Because the areas of IS/OS band disruption in MacTel are discrete and associated with dense scotomas

(Mukherjee et al., 2017), these lesions provide a unique opportunity to assess cone structure and visual function of dysflective cones.

3.3 Methods

3.3.1 Participants

Research procedures followed the tenets of the Declaration of Helsinki. Informed consent was obtained from all participants. The study protocol was approved by the institutional review boards of the University of California, San Francisco and the University of California, Berkeley. Participants with MacTel that had visible disruptions in the IS/OS layer of SD-OCT images within 3 degrees of the foveal center were recruited. Participants were excluded if they had conditions that could affect imaging including unsteady fixation, cataract, greater than 6 diopters myopia, and amblyopia.

3.3.2 Examination procedure

3.3.2.1 Spectral Domain Optical Coherence Tomography (SD-OCT)

Horizontal SD-OCT B-scans (Spectralis HRA + OCT; Heidelberg Engineering, Vista, California, USA) extending 15 degrees by 10 degrees centered on the fovea were acquired with a maximum B-scan interval of 30 microns with the manufacturer's automated retinal tracking feature set between 9-16, in addition to a high resolution horizontal and vertical crosshair scan 30 degrees in length through the foveal center with the manufacturer's automated retinal tracking feature set between 40-100.

3.3.2.2 Adaptive Optics Scanning Laser Ophthalmoscopy (AOSLO) Imaging

An AOSLO system, as described previously, was used to acquire high resolution confocal and split-detector retinal images (Scoles et al., 2014). The simultaneous imaging is useful for two reasons. First, the correction of distortion in each video frame caused by fixational eye movements works better for the high-contrast confocal channel (Stevenson & Roorda, 2005) thereby leading to a higher signal-to-noise image from each video. The same distortion correction can be then directly applied to the videos from the two simultaneously-collected split-detector channels. Second, the confocal and split-detector modalities reveal different structural information. The confocal modality collects direct back-scattered light and is effective for imaging small, intact, waveguiding photoreceptors. The split-detector modality is a form of phase-contrast imaging and can reveal transparent, but refractive features (Guevara-Torres et al., 2020; Scoles et al., 2014). Split-detector imaging is effective for visualizing intact inner segments of cones photoreceptors, even those that do not reflect light normally (Litts et al., 2020; Scoles et al., 2016). Split-detector imaging also generates less ambiguous images of cones in instances where multi-modal-waveguiding in confocal images render them difficult to discern and interpret (Foote, Rinella, et al., 2019; Scoles et al., 2014).

All light sources for the AOSLO were drawn from a supercontinuum light source (SuperK EXTREME, NKT Photonics, Birkerod, Denmark) and a 97-actuator deformable mirror (DM97, ALPAO, Montbonnot-Saint-Martin, France) was used to correct aberrations in the wavefront measured with a custom-built Shack-Hartman wavefront sensor. Videos were acquired at 30 frames per second with a field of view of 1.2 x 1.2 degrees (approx. 360 x 360 micrometer field). Images from a series of overlapping locations along the horizontal meridian were stitched together into a single montage using custom software (Automontage

https://github.com/BrainardLab/AOAutomontaging) (M. Chen et al., 2016). Cone spacing was measured as close as possible to the testing locations using previously described methods (Duncan et al., 2007; Rodieck, 1991). Cone spacing was compared to mean cone spacing values of 37 healthy controls at similar eccentricities (Ratnam et al., 2013).

3.3.2.3 Adaptive Optics Microperimetry (AOMP)

AOMP is a fundus-guided microperimetry system implemented with the AOSLO system described above with 5.5-fold better tracking accuracy than standard clinical fundus guided microperimetry systems (Tuten et al., 2012). AOMP was used to measure visual function with an AO-corrected 3.45-arcmin stimulus (½ the size of a Goldman I stimulus). We used a stimulus wavelength of 543 nm (bandwidth of 22 nm) because that wavelength is equally sensed by the long and middle-wavelength sensitive cones. The stimulus was projected on the retina by modulating the light at appropriate time points during the AOSLO raster scan via a high-speed acousto-optic modulator (AOM) (Brimrose Corporation of America Spark, Maryland, USA). Retinal landmarks were targeting by controlling the timing of the stimulus according the estimated eye motion position (Arathorn et al., 2007; Tuten et al., 2012). The light source used for imaging and eye tracking was 840 nm, while wavefront sensing used 940-nm light. The background light in the system was comprised of the 840-nm and 940-nm channels as well as the small amount of light that leaks through the AOM at 543 nm, even while the switch is off. The combined background was 4 cd/m^2 or 1.65 log Trolands (Td), while the highest intensity 543 nm light was ~3.5 log Td. The stimulus intensity spanned 30 dB by modulating over a range of 1000 linearized steps. The stimulus was delivered for 6 frames per trial (6 brief pulses at 30 Hz) and 30 trials were repeated using a QUEST staircase yes-no thresholding procedure (Watson & Pelli, 1983).

3.4 Results

Three female participants diagnosed with MacTel, 40176 (age 48), 40155 (age 43), and 40150 (age 66), were imaged with AOSLO and tested with AOMP in the eye with better acuity. Participant 40176 had an outer retinal lesion shown in the SD-OCT image at baseline in Figure 3.1C and returned for a follow up visit 12 months later. Participant 40155 had AOSLO imaging of a very small outer retinal lesion close to the fovea shown in the SD-OCT b-scan at follow up 18 months later. Participant 40150 had an outer retinal lesion in addition to several inner retinal cavitations overlying the area as seen in the OCT image in Figure 3.3A and C.

3.4.1 Adaptive Optics Structural Imaging and Microperimetry

The AOSLO confocal montages for participant 40176 are shown in Figure 3.1A (baseline) & D (1 year). The hyper-reflective area in the center of the lesion with a hyporeflective border area is similar to what has been reported previously for MacTel (Litts et al., 2020; Q. Wang et al., 2015). The hyperreflective central regions typically correspond to regions with no visible cones in AOSLO and no inner/outer segment junction (IS/OS) or cone outer segment tip (COST) reflections in OCT. If anything, these regions often have a honeycomb-like scattering profile which is thought to arise from scattering at the junctions of the RPE cells (Roorda et al., 2007). The hyporeflective border regions typically correspond to regions with very weak reflections in the IS/OS and COST bands (Figure 3.1C). For this participant the lesion did not change substantially over 1 year, unlike other reports where structural changes have been observed after 1 year (Litts et al., 2020; Q. Wang et al., 2015). AOSLO split-detector imaging showed mosaics

of inner segments throughout the montage (see insets Figure 3.1B&E). Importantly, the inner segments were visible in some, but not all, of the lesion area. The visible inner segments were largely confined to the border areas of the lesion where the AOSLO confocal images were hyporeflective.

AOMP within the hyper-reflective center of the lesion revealed no measurable function (location ***a*** in Figure 3.1A and B). However, AOMP targeted at the hypo-reflective border (location ***b***) revealed elevated but measurable thresholds, corresponding to reduced visual function, compared to AOMP at a similar eccentricity with healthy-appearing, normo-reflective cones (location ***c*** in Fig 3.1A). The participant's fixation was unsteady during AOMP in the first visit which resulted in rejection of many trials, resulting in a less reliable functional assessment. Nevertheless, during stable fixation the participant saw the stimulus when testing at our maximum amount of light delivery and so the threshold is listed as 1 (ie maximum light delivery was detected) at location ***b***.

AOSLO split-detector imaging (inset, Figure 3.1B) revealed inner segments at the border where there was reduced but measurable function, but there were no inner segments visible within the hyper-reflective center of the lesion where the patient did not see the brightest stimulus delivered. Figure 3.1D-E show a similar result obtained 12 months later, again revealing that the region where intact inner segments were observed had measurable function whereas regions with no visible inner segments did not. In the second session the participant's fixation was much more stable giving a more accurate threshold assessment at location ***b*** than at baseline. After 12 months the lesion did not increase in area and no reflectivity changes were visible in the confocal AOSLO images.

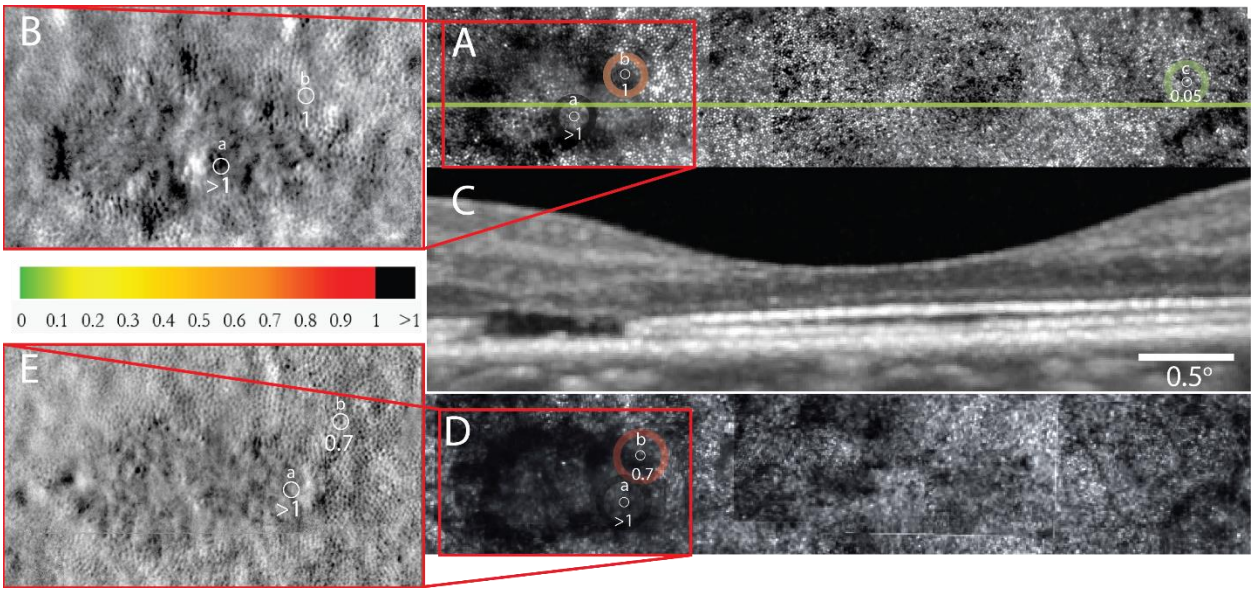

Figure 3.1 Images and microperimetry from baseline (A-C) and after 12 months (D-E) in participant 40176. (A) Confocal image with the 3 testing locations *a*, *b* and *c*. Each location's threshold is shown below the testing location and colors correspond to thresholds on the color bar. The actual size of the stimulus is indicated by the white open circle at each test location circle. The green line through the confocal image indicates the position of the SD-OCT B-scan shown in panel C. The inset panel B is a split-detector image that reveals image inner

segments beneath test location *b*, but not *a*. Confocal images 12 months later are shown in panel D with the split-detector inset shown in panel E.

Participant 40155 had an outer retinal lesion as seen on confocal AOSLO images at baseline (Figure 3.2A) and at followup (Figure 3.2B). The outer retinal lesion appears in the SD-OCT B-scan as an abrupt loss of the OS/RPE band with disruption and dimming of the IS/OS band (Figure 3.2C). Baseline AOSLO imaging revealed intact inner segments within the hyporeflective confocal AOSLO region (Figure 3.2D&E). After 18 months there were small changes in the size and appearance of the lesion (compare Figure 3.2D & F). The area without recovered reflectivity had visible inner segments (Figure 3.2G), although they were not as distinct as in other areas, possibly due to scattering of the image beam at the edges of the overlying inner retinal cavities. AOMP within the lesion at stimulus location ***a*** showed measurable but slightly elevated thresholds compared to location ***b***, a region on the opposite side of the foveal center with healthy appearing cones.

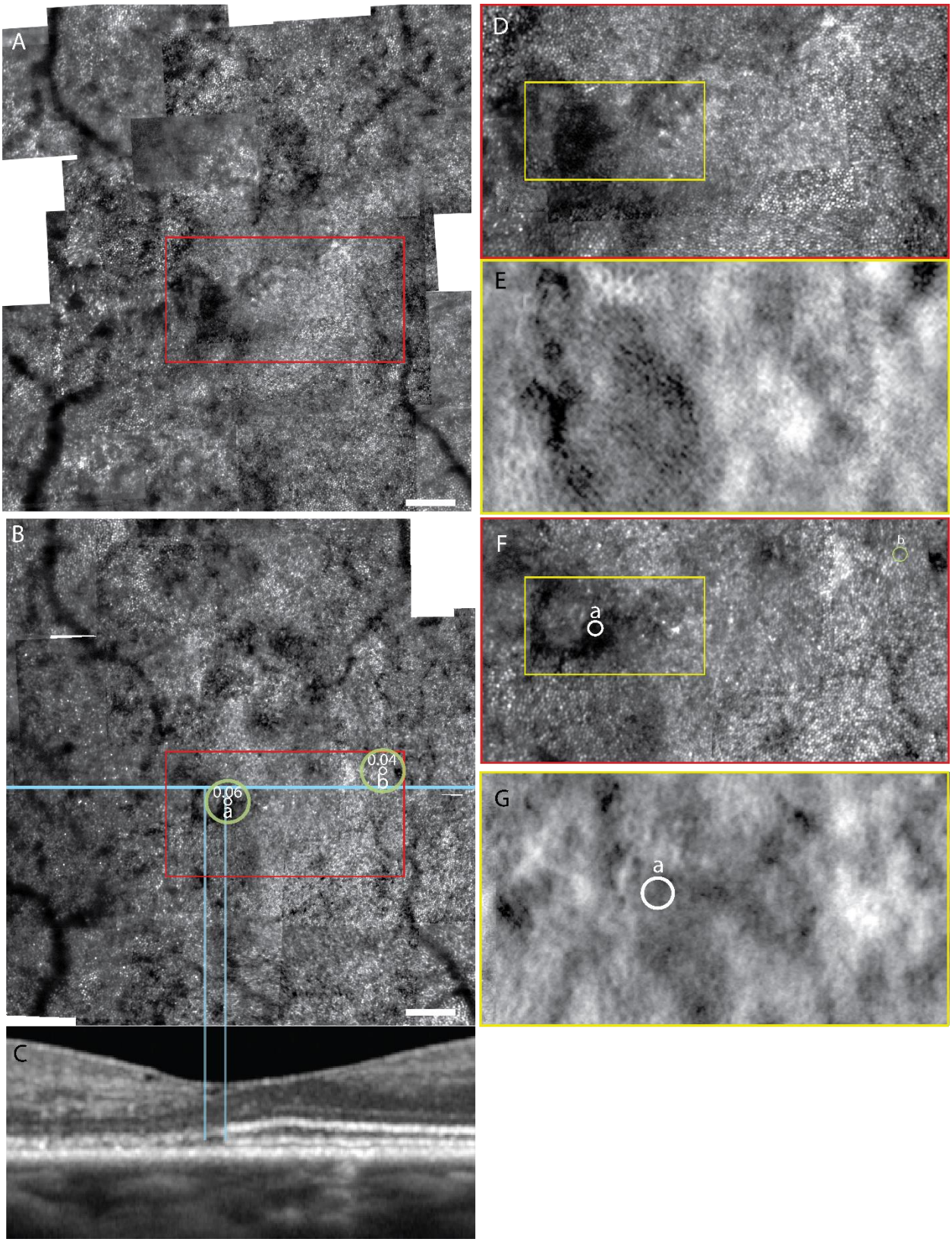

Figure 3.2 Images and microperimetry results for participant 40155. Panel A is the confocal image taken at the first visit. Panel B is the confocal image from the same location taken at

the second visit with testing locations *a* in the hyporeflective area and *b* in healthy appearing area on the opposite side of the foveal center. Panel C is the OCT B-scan from the location indicated by the blue line in the confocal image. Corresponding points between the B-scan and the confocal image are indicated by the vertical blue lines. Panels D and F are enlarged inset from Panels A and B respectively. Panels E and G are further-enlarged split-detector images from Panels D and F respectively. Test locations *a* and *b* are indicated in Panels B and F and only test location *a* is indicated in Panel G. Scale bar is 0.5 deg.

Participant 40150 had extensive inner retinal cavitations overlying a distinct and smaller region of IS/OS junction band disruption (Figure 3.3A and C). Shadows cast by the edges of inner retinal cavitations obscured some details of the confocal AOSLO montage, but there were no unambiguous cones at stimulus location ***a*** (black circle) or ***b*** (orange circle) in Figure 3.3B. The SD-OCT B-scan image (Figure 3.3A, corresponding to the blue line in figure 3B) shows an IS/OS break at AOMP stimulus location ***a*** and IS/OS disruption in stimulus location ***b*** (Figure 3.3C, corresponding to the green line in Figure 3.3B). The split-detector inset corresponding to stimulus location ***a*** where the brightest stimulus was not seen showed no intact inner segments in or around the stimulated area, whereas inner segments were visible in and around stimulus location ***b*** with measurable function (Figure 3.3D).

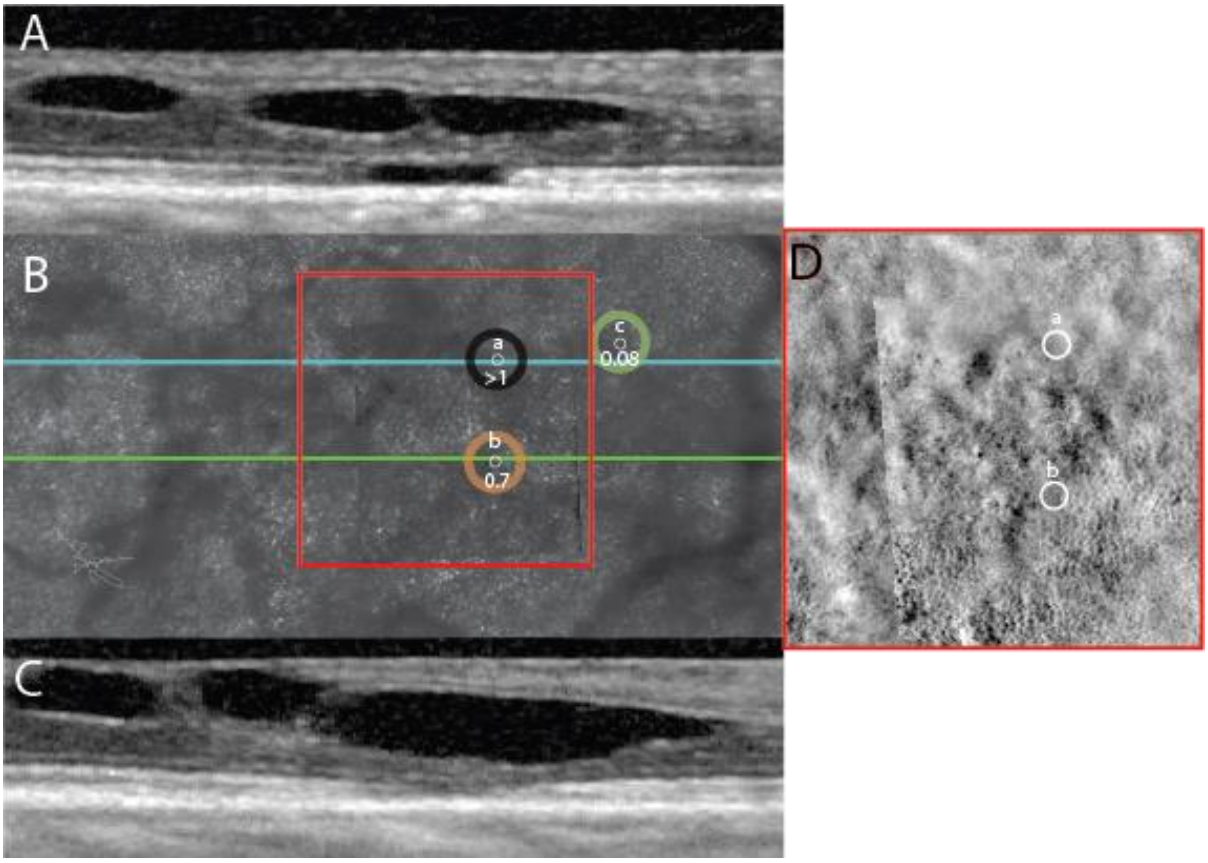

Figure 3.3 Images and microperimetry results for participant 40150. Panel A is the SD-OCT B-scan at the blue line in the confocal image in panel B that passes through location *a* where the brightest stimulus was not seen. Panel C is the SD-OCT B-scan at the green line of the

confocal image that passes through test location *b*. Panel D is the split-detector image where inner segments can be seen at test location *b* but not at *a*.

3.4.2 AOSLO Cone Spacing

Cone spacing was measured in the dysflective area with visible inner segments (location ***b*** in participant 40176 shown in Figure 3.1, location ***a*** in participant 40155 shown in Figure 3.2, and location ***b*** in participant 40150 shown in Figure 3.3). Cone spacing was also measured at the stimulus location with normal-appearing cones on confocal imaging at equivalent eccentricities (location ***c*** in participant 40176 shown in Figure 3.1, location ***b*** in participant 40155 shown in Figure 3.2, and location ***c*** in participant 40150 shown in Figure 3.3). Split-detector images were used to label cones and measure their spacing inside dysflective areas, while confocal images were used to measure cone spacing for locations with normally reflective cones at equivalent eccentricities outside dysflective areas. Figure 3.4A & B show these cone spacing measures in arcminutes with at least 30 cones selected per location; cone selections for participant 40176 are shown in Figure 3.4C. Cone spacing measured in split-detector images inside the dysflective areas (Figure 3.4A & B, orange) was greater than 2 standard deviations above healthy normal cone spacing, while confocal images from healthy appearing cones outside the dysflective areas (Figure 3.4A & B, blue) followed the healthy participant trendline with eccentricity shown in Figure 3.4B. Cone spacing in the confocal images of the healthy appearing locations outside the dysflective lesions, while lower in all but 40155, was not significantly different from cone spacing measured in split-detector images of dysflective cones in MacTel lesions.

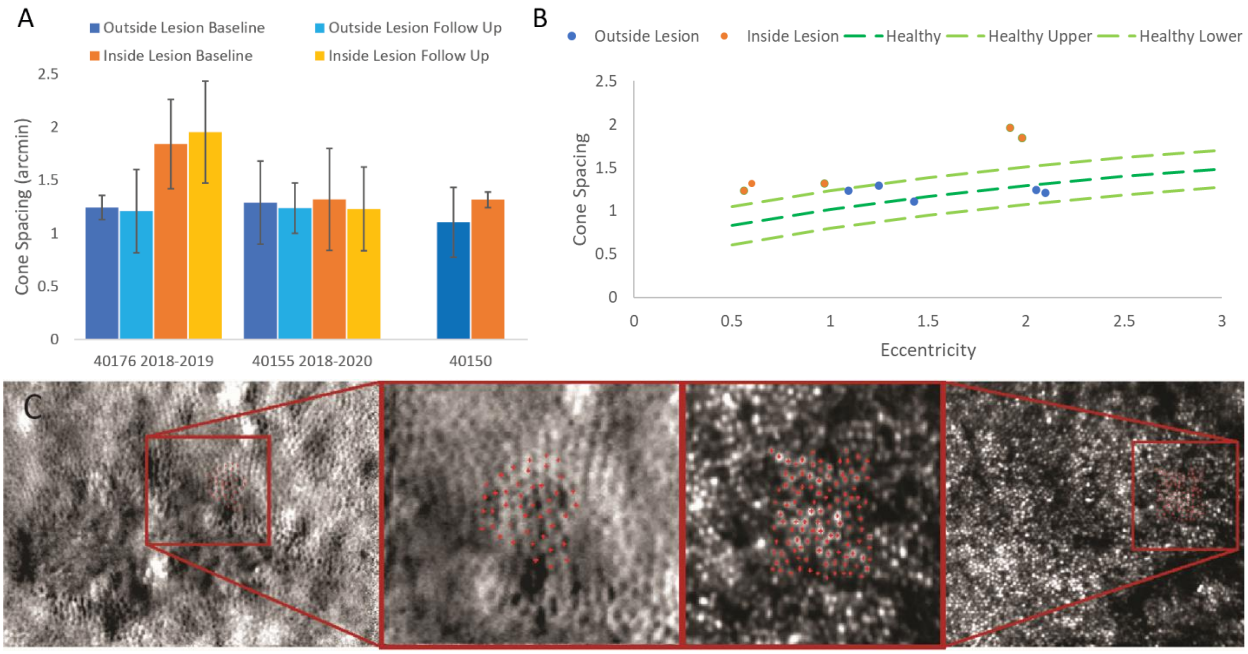

Figure 3.4 Cone spacing measurements from each participant and each imaging date. Cone spacing at the dysflective area within the lesions shown in blue (location *b* in participant 40176 shown in Figure 3.1, location *a* in participant 40155 shown in Figure 3.2, and location *b* in participant 40150 shown in Figure 3). Cone spacing with normal-appearing cones at equivalent eccentricities are shown in orange (location *c* in participant 40176 shown in Figure 3.1, location *b* in participant 40155 shown in Figure 3.2, and location *c* in participant 40150

shown in Figure 3.3). Error bars are the 95% confidence limits of the cone spacing estimate. (B) Cone spacing as a function of eccentricity for MacTel dysflective areas within lesions shown in orange, MacTel healthy appearing areas in blue. The three dashed line are the average and upper and lower 95% confidence limits of cone spacing as a function of eccentricity from a cohort of healthy control eyes. (C) Cone selection locations are shown as red crosses for 40176 in 2018 with the split-detector image of the lesion on the left and confocal image on the right with zoomed in insets of each location.

3.5 Discussion

In this study, we showed that dysflective cones in MacTel lesions (i.e. regions where cones are hyporeflective and not visible in AOSLO confocal images but that have measurable visual function) correspond to regions where the cone inner segments are visible in split-detector images. Cone spacing in the dysflective areas of the MacTel lesions was slightly above normal, falling outside the upper 95% confidence limit of healthy controls.

Areas that did not have visible cones in confocal or split-detector images did not have measurable function, indicating a link between remnant cone inner segments and measurable, but often reduced, function (ie high thresholds). These structural findings are consistent with recent AOSLO split-detector imaging done by Litts et al. 2020 and with histological findings of intact cone inner segments in Mactel lesions with no IS/OS reflectivity on OCT (Powner et al., 2013). In participant 40176 the outer retinal lesion did not change over the year and neither did the function. However, participant 40155 had areas with recovered reflectivity over 18 months similar to recovered reflectivity shown previously (Litts et al., 2020; Q. Wang et al., 2015). Given that previous natural history studies have shown an increase of IS/OS Mactel lesion size of 0.14 mm over a two year period it is surprising that we did not see an increase in lesion area in either patient over 1 year (40176) and 18 months (40155), however the lesions in this study were very small and may behave differently compared to those that have been described in previous publications (Sallo, Peto, Egan, Wolf-Schnurrbusch, Clemons, Gillies, Pauleikhoff, Rubin, Chew, Bird, et al., 2012).

AOSLO microperimetry measurements identified clear areas where we were unable to deliver enough light for the participant to see the stimulus. An unmeasurable threshold in some parts of the lesion was also observed in one of the participants reported in Wang et al.(Q. Wang et al., 2015) It is possible, though unlikely, that the participant may have perceived the stimulus if the maximum intensity was higher. The maximum stimulus intensity in this study was approximately 1/5 the maximum stimulus intensity used in Wang et al.(Q. Wang et al., 2015) This lower stimulus intensity was necessary for proper threshold measurements at normal-appearing cone testing locations, which had about a 10x lower threshold in both participants compared to the lesioned areas. In Wang et al.(Q. Wang et al., 2015) the normal appearing cone testing locations had a 5x lower threshold compared to lesioned areas, potentially from increased deliverable intensity step sizes.

SD-OCT B-scans revealed clear loss of the IS/OS junction in all 3 participants, however there was no clear feature within the B-scans that help to differentiate dysflective areas from those with no measurable function in 40176 or 40150. In participant 40150 the OCT scan of the dysflective area at location ***b*** has no evidence for an intact ELM, however the OCT scan of the region with no measurable function at location ***a*** shows remnant ELM. In participant 40176 the scan that is closest to the region with no measurable function also has an intact ELM. This is

surprising given that Wang et al.(Q. Wang et al., 2015) showed measurable function specifically in areas with an intact ELM and Litts et al.(Litts et al., 2020) showed that there was an intact ELM in all their participants who recovered reflectivity over time. Participant 40150's results are complicated by the large inner retinal cavitations and it is possible that if higher stimulus intensities were available in our AOMP system a threshold might have been measured.

Cone spacing was within normal limits for all participants outside of the lesion but was more than 2 standard deviations above normal within the dysflective area of the lesions. This increase in cone spacing may explain the decreased visual sensitivity (increased thresholds) from AOMP since it has previously been shown that macular sensitivity measured with MAIA microperimetry correlated with cone spacing in both subjects with retinal degeneration and normal subjects (Foote, Huerta, et al., 2019). For the 2 participants whose cone spacing was measured at two times separated by more than one year, there was no clear increase in cone spacing inside or outside the lesion. This is unlike what shown in Litts et al in 7 subjects over the same time period, however this could be due the difference in the number of participants (Litts et al., 2020).

3.6 Conclusion

Dysflective cones have previously been defined as cones that are not visible in confocal AOSLO images or in OCT but have measurable sensitivity (Q. Wang et al., 2015) and spatial vision (Tu et al., 2017). In this paper, we showed that cones were indeed present in these dysflective regions and their inner segments could be seen with AOSLO split-detector imaging, a form of phase-contrast imaging. This is an important state of cone health to identify, as these are cones that might be most amenable to full recovery, either spontaneously (Q. Wang et al., 2015) or through treatment.

Contents of this chapter are in prep for submission: Bensinger, E, Wong, J, Roorda AJ, Duncan JL. Dysflective Cones in Macular Telangiectasia Lesions

Chapter 4 | Dysflective Cones at Eccentric Fixation in Subjects with Macular Atrophy

4.1 Abstract

Four eyes of 4 patients with macular atrophy due to congenital rubella, Best macular dystrophy, macular atrophy associated with cuticular drusen, and Stargardt's disease were studied using AOSLO, OCT, and fundus-guided microperimetry to track the structure and function relationship within the area of the preferred retinal locus (PRL). Cones at the PRL were not visible in confocal images but showed measurable sensitivity indicating these are dysflective cones. Fixation was within the dysflective region despite normal-appearing and more sensitive cones at greater eccentricities. OCT showed intact external limiting membranes but hyporeflective inner segment/outer segment junctions. The PRL was relatively stable over time: 2 subjects changed <0.1° over 1 year and 1 changed 1.8° over 8 years. Participants used and maintained an eccentric PRL with dysflective cones despite more sensitive and normal-appearing cones at greater eccentricities, indicating proximity to the anatomic fovea is more important than cone reflectivity and sensitivity in determining the PRL location.

4.2 Introduction

The part of the retina where images are placed during fixation is called the preferred retinal locus (PRL) and, in participants without central vision loss, the PRL generally coincides with the anatomical fovea. Close inspection, however, has revealed that the anatomical fovea is not well defined: the base of the foveal pit, the point of peak cone density, and center of the foveal avascular zone are all close to each other but never perfectly aligned. Moreover, multiple groups have found that the PRL rarely corresponds to any of these landmarks (Kilpeläinen et al., 2020; Li et al., 2010; Putnam et al., 2005; Reifniger et al., 2019; Wilk et al., 2017). The PRL in healthy individuals, for example, is very consistent between measurements and over days (Kilpeläinen et al., 2020) but does not correspond exactly to the point of highest cone density (Putnam et al., 2005).

Development of a PRL for eccentric viewing is one of the functional adaptive mechanisms that follows irreversible central vision loss resulting from macular atrophy (Cheung & Legge, 2005). The PRL is forced to shift due to a lack of sensory input from the original foveal region and the PRL location changes with progressive change in the atrophic lesion. The PRL may be located at the edge of the atrophic lesion in eyes with age-related macular degeneration (AMD)(Crossland et al., 2005; Krishnan & Bedfell, 2018; Timberlake et al., 1986, 2005) but in other retinal degenerations, including Stargardt disease, there have been reports of a space between the edge of the atrophic lesions and the PRL(Greenstein et al., 2008; Rohrschneider et al., 2008; Verdina et al., 2017).

The fixation stability as measured by the area of a best-fitting bivariate contour ellipse that contains 68% of the fixation positions (BCEA) in participants with macular atrophy has previously been reported to be larger in eccentric fixators compared to healthy age-matched participants(Kumar & Chung, 2014). The PRL is usually located close to the foveal center in retinal areas with preserved function, and can be located at anatomical locations that are superior, nasal or temporal to the fovea, but is rarely located inferiorly(Messias et al., 2007; Verdina et al., 2017). The PRL in participants with central scotomas are known not to be always in the location of highest visual acuity or in the location with greatest retinal sensitivity(Greenstein et al., 2008).

Understanding the PRL is important for evaluating and planning rehabilitation strategies for participants with central vision loss(Erbezci & Ozturk, 2017), but the anatomic and functional characteristics of such retinal locations are not fully understood, perhaps in part because most clinical tools used to evaluate the PRL have not had sufficient resolution to visualize individual cells mediating fixation and acuity. Multiple reports have been published to assess the structural and functional characteristics of the PRL using scanning laser ophthalmoscopy (SLO), spectral-domain optical coherence tomography (SD-OCT), fundus autofluorescence (FAF) and microperimetry(Crossland et al., 2005; Erbezci & Ozturk, 2017; Greenstein et al., 2008; Krishnan & Bedell, 2018; Messias et al., 2007; Shima et al., 2010; Verdina et al., 2017). A brief summary of those reports is that the PRL can be associated with regions that have intact inner segment/outer segment (IS/OS) junction or ellipsoid zone (EZ) bands, intact external limiting membranes (ELM) and relatively normal FAF (Verdina et al., 2017).

Adaptive optics scanning light ophthalmoscopy (AOSLO) is a modality that can generate cellular-resolution images in the macula of living eyes (Roorda et al., 2002) and that can identify the PRL with micrometer-scale accuracy (Li et al, 2010, Wang et al 2019). To date, the use of AOSLO to study the PRL and its underlying retinal structure and function in eyes with macular atrophy is limited to a single case (Tu et al., 2017).

In this study, we employ a multi-modal, high-resolution imaging approach to characterize the PRL in participants with macular atrophy arising from four different conditions. Modalities include AOSLO, SD-OCT, swept-source OCT angiography (OCT-A), FAF and fundus-guided microperimetry to more clearly understand the relationship between retinal structure and function at the PRL.

4.3 Methods

4.3.1 Study participants

Approval for this study and data collection was obtained from the Institutional Review Board of the University of California, San Francisco. The study was carried out in accordance with the Declaration of Helsinki. Written informed consent was obtained from each study participant. Eyes with macular atrophy and visual acuity of 20/40 or better were selected for detailed study. We studied 1 eye each of 4 participants, one with congenital rubella (Participant 1, 40122), one with Best vitelliform macular dystrophy (Participant 2, 40146), one with macular atrophy associated with cuticular drusen (Participant 3, 40184), and one with Stargardt disease associated with compound heterozygous pathogenic variants in the *ABCA4* gene (Participant 4, 30014) (Table 1). 12 participants with retinitis pigmentosa, 8 with *USH2A* mutations and 4 with *RHO* mutations (previously reported in Foote et al. 2020) with visual acuity 20/50 or better were selected for comparison to our macular atrophy participants (Foote et al., 2020).

4.3.2 Genetic analysis

A saliva sample was acquired for genetic testing from participants 40146, 40184, and 30014 as well as the comparison participants with retinitis pigmentosa. Genetic testing was done using a next generation sequencing panel which included 181 genes (Blueprint Genetics, Helsinki, Finland) from 40146 and 40184. All 50 exons of the *ABCA4* gene were sequenced on a research basis using the Illumina (San Diego, CA) platform in 30014, as previously reported(Chen et al., 2010). Genetic testing was performed using an amplification refractory mutation system for the

most common RP-causing variants in the *RHO* gene on a fee-for-service basis (Carver Nonprofit Genetic Testing Laboratory, Iowa City, IA) in 30019; with a 67 gene retinal dystrophy next generation sequencing panel on a fee-for-service basis (EGL Genetics Laboratory, Tucker, GA) in 40163; with a 13 gene autosomal recessive RP panel (Oregon Health & Sciences University, Portland, OR) in 40082; with a 9 gene Usher syndrome panel in 40097 (GeneDx, Gaithersburg, MD), analysis of the 5 coding exons and the flanking intronic regions of the *RHO* gene (40095, 40183) (University of Texas-Houston), or a 266 gene next generation sequencing panel (40167) (Ocular Genomics Institute, Massachusetts Eye and Ear Infirmary, Boston, MA) through the eyeGENE research consortium (Sullivan et al., 2013); or using a next-generation sequencing retinal dystrophy panel with deletion/duplication analysis through the My Retina Tracker® registry genetic testing study (NCT 02435940) (181 genes: 40039, 40151, 40110 and 40153; or 266 genes: 40180). Participants with autosomal recessive RP associated with likely pathogenic or pathogenic variants in the *USH2A* gene submitted samples from at least 1 first degree relative to confirm inheritance was *in trans.*

4.3.3 Examination procedure

Visual acuity was measured according to the Early Treatment of Diabetic Retinopathy (ETDRS) protocol(Ferris III, Frederick L, Kassoff & Bailey, 1982). SD-OCT, infrared fundus photographs, and FAF (Spectralis HRA + OCT; Heidelberg Engineering, Vista, California, USA) images were obtained in all 4 participants with macular atrophy.

4.3.4 Optical Coherence Tomography-Angiography

High resolution vascular images were acquired using a swept-source OCT-A system (PLEX Elite 9000; Carl Zeiss Meditec Inc., Dublin, CA, USA) in all 4 participants with macular atrophy. Three-dimensional slab images were obtained by scanning a 6mm x 6mm area in a horizontal raster plan as described previously(Rosenfeld et al., 2016). Choriocapillaris flow voids within and around the PRL were quantified as previously described(Q. Zhang et al., 2018) and summarized briefly as follows. The optical microangiopathy (OMAG ®) algorithm was used to identify blood flow in the scans. A semi-automated segmentation algorithm was used to identify the choriocapillaris slab, which extended from the outer border of the Bruch's membrane (BM) to about 20 μm below BM. A new algorithm which comprised pre-processing and signal compensation was applied to the *en-face* choriocapillaris slabs to compensate for choriocapillaris signal attenuation imposed by the structural changes in the RPE/BM complex. After setting the threshold at 1 standard deviation below the mean choriocapillaris flow of a database comprised of 20 normal participants, the flow void percentages within and around the PRL were estimated in a 2 degree grid pattern throughout the macula, excluding areas of atrophy from the analysis.

4.3.5 AOSLO imaging

High-resolution images of cone photoreceptors in the central macular area of 5.7-degree diameter were obtained using confocal AOSLO and the digital videos were processed with the aid of custom image analysis software (MATLAB, The MathWorks, Inc., Natick, MA, USA) and montages were assembled were assembled using custom software (Automontage; https://github.com/BrainardLab/AOAutomontaging) (M. Chen et al., 2016).

4.3.6 AOSLO-based PRL Determination and Fixational Analysis

The exact location of the PRL was determined using a feature of the AOSLO whereby a fixation

target is presented to participants via direct projection within the raster scan. For this particular study, the fixation target was created by turning off the laser at a fixed locations within the raster scan to present a black circle 0.12 degrees in diameter blinking at 6 Hz within the raster-scanned field (Poonja et al., 2005). A fixation target so delivered is encoded directly into the AOSLO video and so the PRL used for fixation can be determined with absolute certainty (Li et al., 2010). PRLs were determined for the four eccentric-fixating participants based on a 10-second video recording of the retina with the fixation target.

A more extensive quantification of fixation stability was obtained by extracting high-frequency eye motion traces from additional AOSLO videos that were used to generate the montage images (Stevenson & Roorda, 2005). In these videos, the fixation target was not delivered via the raster as above but it was a white cross (~ 0.2 deg in size) on a black background presented with a second display that was viewed through a beamsplitter in the AOSLO system. This is the fixation target that is generally used to collect the AOSLO videos that are used to build the large-field montages of the retina. During imaging, participants are instructed to fixate as steadily as possible on the white cross over the course of each video. Ten eye motion traces were extracted from AOSLO videos so collected from each participant. From the eye motion traces for the four macular atrophy participants the BCEA containing 68% of fixation was calculated. The BCEA was then compared with those similarly collected from a group of 4 healthy, age-similar participants, 4 participants with RP due to pathogenic mutations in the *RHO* gene, which is expressed exclusively in rods, and 8 participants with retinal degeneration associated with pathogenic mutations in the *USH2A* gene, which is expressed in rods and cones. Participants were divided into 2 groups based on visual acuity: BCVA <20/30, and a BCVA 20/30-20/50 with their clinical information shown in Table 1.

4.3.7 Microperimetry

Fundus-guided microperimetry (Macular Integrity Assessment (MAIA), CenterVue, Fremont, CA) was used to measure macular sensitivities across a predefined set of locations in all participants. A dense custom grid extending every 1^o from central fixation at least 4^o in the superior, inferior, nasal and temporal axes was used to assess macular sensitivity around the PRL and in regions corresponding to high-resolution SD-OCT scans from the horizontal and vertical meridians from the PRL. A less dense 10-2 full threshold strategy comprising a 68-stimuli grid covering the central 20^0 of the retina was used to determine retinal sensitivities in RP participants. Measurements were made in a semi-dark room using a Goldmann III stimulus presented for 200 ms. The background luminance was 1.27 cd/m^2 with a maximum stimulus luminance of 318.47 cd/m^2. MAIA uses 25 Hz eye-tracking to guide the delivery of the test stimuli as well as to monitor fixation.

The MAIA offered independent measures of the PRL and fixation stability for each participant. During a MAIA measurement, participants are asked to hold fixation in the center of a 1^o-diameter red circle. The instrument uses all fixation positions over the course of the entire test to generate fixation indexes, which represent the percentage of fixation points inside a circle of 2^o and 4^o diameter, respectively. Participants are classified as having stable fixation if greater than 75% of the fixation points are within 2^o, relatively unstable fixation if less than 75% of the fixation points are within 2^o and greater than 75% are within 4^o, and unstable fixation if less than 75% of fixation points are within 4^o (MAIA, 2011). Additionally MAIA analyzes fixation by computing the BCEA containing 63% of the fixation points during the scan, with the scan duration averaging 10 minutes in our participants.

4.3.8 Combining the Data

All images and fundus-landmarked functional data from all structural and functional tests were aligned with each other manually using vascular landmarks and were assembled into overlays in Adobe Illustrator (Adobe Systems, San Jose, CA, USA). Since the participants had central scotomas, and the foveal structure (including the shape of the foveal pit) was compromised, the anatomic fovea was identified as the center of the foveal avascular zone on OCT-A images of each study eye.

4.4 Results

4.4.1 Structural Measures

Clinical information is summarized in Table 1 with ages for participants 40122, 40146, 40184 and 30014 given for the most recent imaging visit with an age range 26-57. Visual acuities in the study eyes ranged from 20/20 to 20/40. A heterozygous, likely pathogenic, mutation in the *BEST 1* gene (c. 920 C>T; p. Thr307Ile) was identified in Participant 40146. A single heterozygous nucleotide change (c.4457C>T, p.Pro1486Leu; c.3759), one novel heterozygous insertion (c.672ins6bp) and one novel heterozygous deletion (c.672del32bp) were identified in the *ABCA4* gene in 30014, as previously described (Chen et al., 2010). No disease-causing genes were found in 40184.

Participants 40122 and 40184 were imaged twice with one year between imaging sessions, and participant 30014's imaging sessions were 8 years apart. The PRL was located superonasal to the anatomic fovea in 40122 and superotemporal to the anatomic fovea in 40146, 40184, and 30014 in most recent images (below A-D). SD-OCT B-scans showed the external limiting membrane band (ELM) was visible overlying hyporeflective, disrupted inner segment/outer segment junction or EZ bands and cone outer segment tip, or interdigitization zone, bands at the PRL in each study eye (below A-D); The BCEA defined by microperimetry (red dashed circles, below M-O) was larger than, and did not exactly match the location of the BCEA determined by AOSLO (blue ellipse, Figure 1 E-H). MAIA estimates of BCEA are not shown for 30014 due to unstable fixation measurement. The PRL was located between 0.4-1.9 degrees from the anatomic fovea in all 4 eyes in the most recent images. Participants 40122 and 40184 did not change the location of their PRL over 1 year (below Q, S). The PRL 30014 coincided with the anatomical foveal at the first visit (belowR), but 10 years it had shifted 1.92^{o} superiorly. Unambiguous cones were not visible at the PRL in confocal AOSLO images in any participants, even though more normal-appearing cones were located elsewhere in the images at greater eccentricities than the PRL.

RPE structure and choriocapillaris perfusion were also abnormal at the PRL. FAF showed reduced and/or heterogeneous autofluorescence at the PRL in all 4 eyes (below A-D). SS-OCTA images of choriocapillaris flow void in the macular area imaged in normal eyes has been reported as 10.31 ± 3.66% (Q. Zhang et al., 2018). Choriocapillaris flow void within the PRL in most recent images was normal in 40146 (7%) and 40122 (12%), but was increased in 40184 (17%) and 30014 (40%) (below I-L). We point out here that participant 40184 opted for a PRL with increased flow void even though there were regions at similar eccentricities to the anatomical fovea that had more normal choriocapillaris coverage (e.g. ~10% at a three nasal locations in below L).

4.4.2 Functional Measures

Mean retinal sensitivities in normal healthy eyes using MAIA have been previously reported as 29.26 dB, 28.19 dB and 27.31 dB respectively at $0\text{-}2^0$, $2^0\text{-}6^0$ and $6^0\text{-}10^0$ from fixation (Parodi et al., 2015). Mean retinal sensitivities were abnormal at several locations throughout the macula in 40122, 40146, and 40184, and were severely reduced at the PRL at 17 dB, 17 dB and 19 dB, respectively (below M-P). 40122, 40146, and 40184 maintained fixation within 2^0 of the target between 96 and 100% of the time (below M-P). Participant 30014 did not appropriately attend to the task during the most recent MAIA session with a relatively unstable fixation (MAIA BCEA 5.3 degrees) and 8/12 targets to the optic nerve marked as seen, and so retinal sensitivities were not reliable enough to report.

4.4.3 Fixational Measures

BCEA measured by the AOSLO was analyzed in 10 eye motion traces from each of the participants in these 5 groups: eccentric fixation participants, participants with *USH2A*-related RP and visual acuity better than 20/25, *USH2A*-related RP participants with visual acuity 20/50–20/30, participants with *RHO*-related RP, and healthy participants. BCEA results in degrees squared are shown in below. There was no significant difference between participants with eccentric fixation and participants with RP regardless of visual acuity (P=0.11 for comparison to *USH2A* with BCVA equal to or better than 20/25, P=0.27 for comparison to participants with *USH2A* with BCVA equal to or worse than 20/30, and P=0.07 for comparison to participants with *RHO* mutations). There was a significant difference in BCEA between participants with eccentric fixation and healthy participants (P=0.002). There was no significant difference between any groups in age, and when combining all groups, neither age nor visual acuity were significantly correlated with BCEA. Retinal sensitivity at the PRL measured in MAIA for all groups except healthy controls was also not significantly correlated with BCEA.

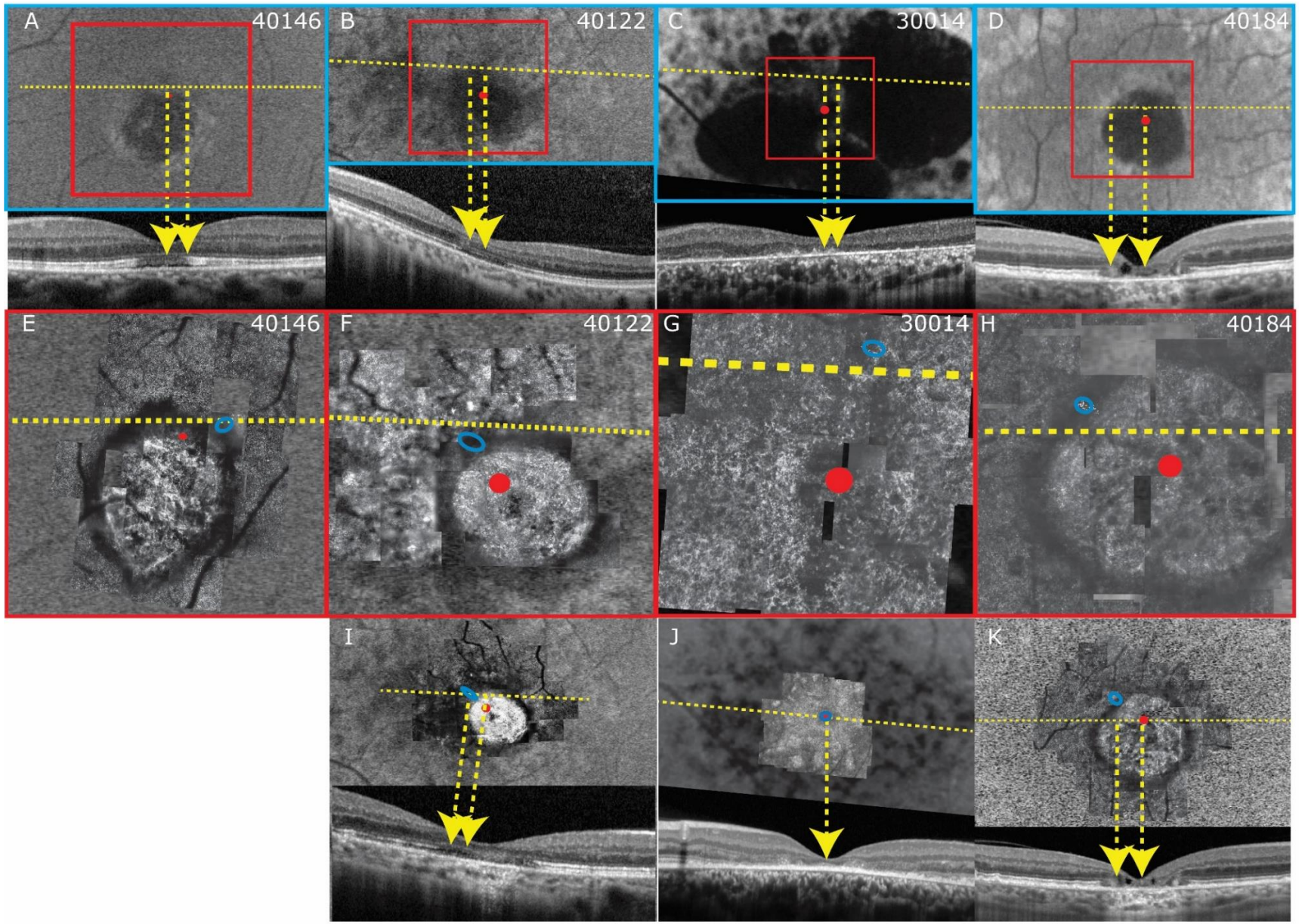
A
40146
B
40122
C
30014
D
40184
E
40146
F
40122
G
30014
H
40184
I
J
K

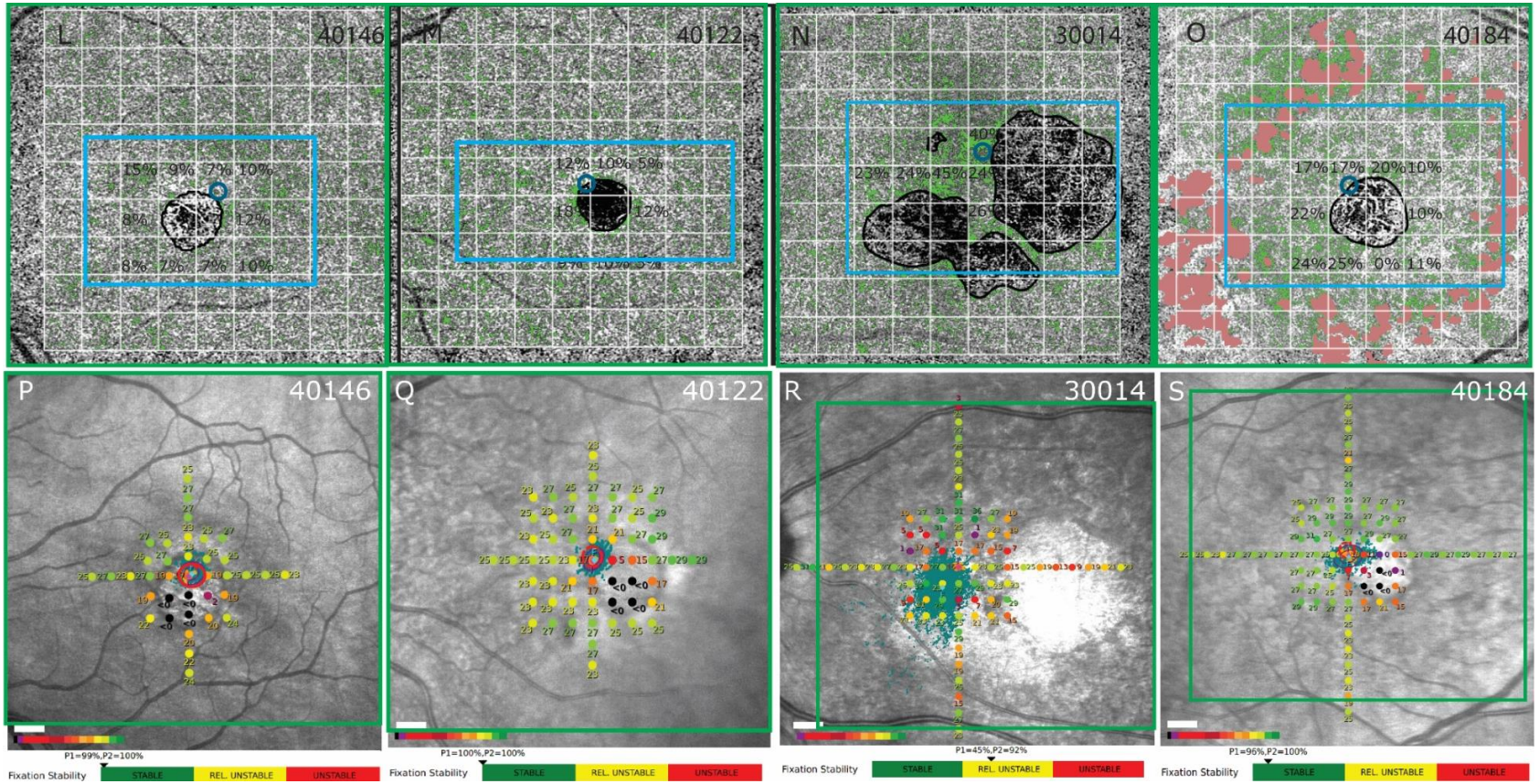

Figure 4.1: Imaging results from participants with Eccentric PRLs at follow up in panel A-H and at baseline in panels I-K. Panels A-D show the FAF images with the OCT B-scans shown below corresponding to the yellow dashed lines. Panel's E-H show the AOSLO images corresponding to the region in the red square in panels A-D. Red circles indicate the locations of the anatomic fovea while blue ellipses correspond to the PRL. Panel's I-K show the baseline imaging session with the AOSLO overlayed over the FAF and the SD-OCT B-scan shown below. Panels L-O show the OCTA flow void results with the blue rectangle corresponding to the region in the FAF images in panels A-D. OCTA flow voids are marked by green dots for each macular atrophy patient. Images are broken up into 2^{o} grids with flow void percentages shown for the areas around the atrophy. Red areas marked in 40184 indicate areas with drusen. Panel's P-S show the MAIA sensitivity levels in decibels marked by the colored circles. Fixation locations are shown by green dots with the BCEA for all subjects except 30014 (due to unsteady fixation) shown by the red ellipse. The MAIA fixational stability is indicated at the bottom of each panel. The green rectangles correspond to the regions in the OCTA images in panels L-O

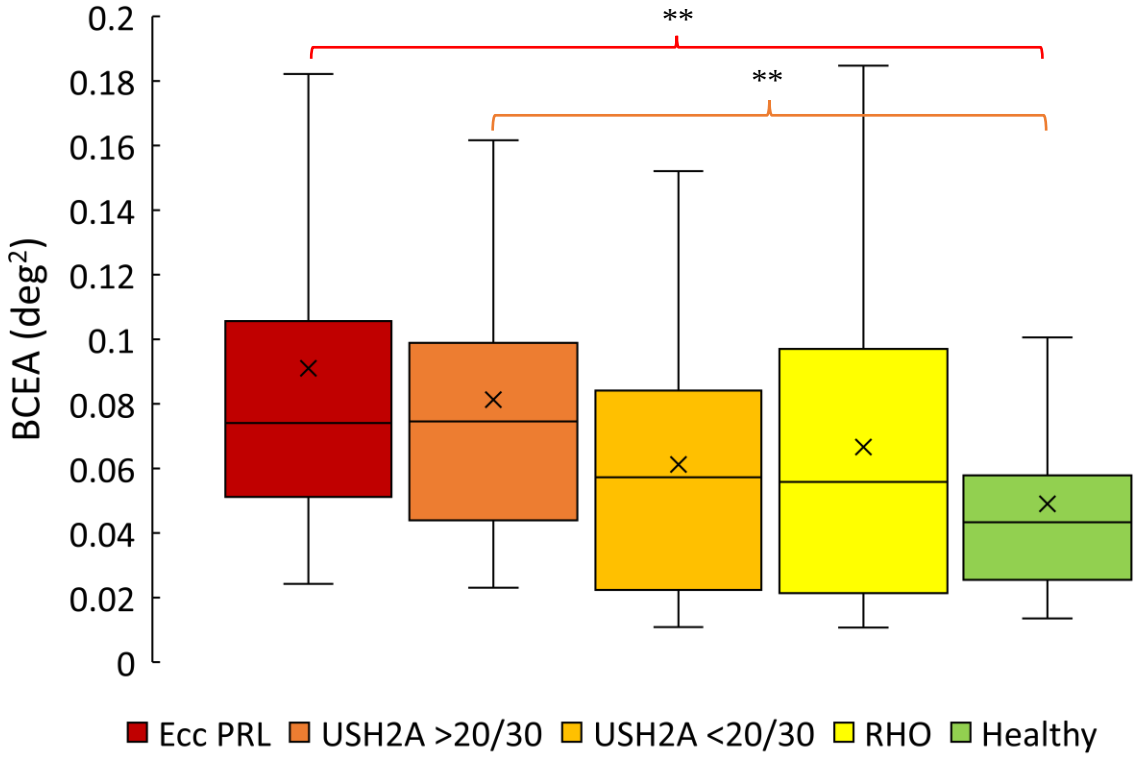

Figure 4.2: AOSLO BCEA measurements in degrees for macular atrophy subjects with eccentric PRL (red), USH2A mutation retinitis pigmentosa subjects with visual acuity worse than 20/30 (dark orange) and better than 20/30 (orange), RHO mutation retinitis pigmentosa subjects (yellow), and healthy subjects (green). Significant differences are marked by asterisks with ** indicating P<0.01.

BCEA for eccentric fixating participants 40146, 40184, and 30014 were not significantly different from one another, but all three had significantly lower BCEA than participant 40122 with congenital rubella. Participant 40122 and 40184 did not change BCEA significantly over a 1 year period as shown in Figure 4.3.

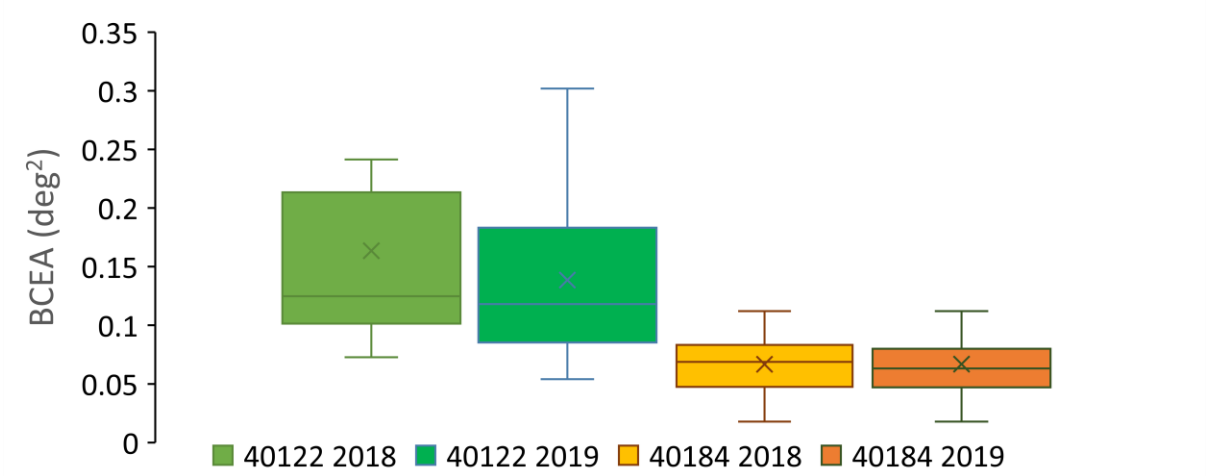

Figure 4.3: AOSLO bivariate contour ellipse area measurements for subjects 40122 with rubella and 40184 with cuticular drusen at baseline and follow up 1 year later.

4.5 Discussion

4.5.1 Location of PRL

Using a multi-modal, high-resolution imaging approach, the present study of the PRL in participants with macular atrophy from 4 different conditions demonstrated that proximity of the PRL to the anatomic fovea is more important than integrity of retinal structure or function at the PRL. In 4 out of 4 cases of macular atrophy due to different causes, participants used a retinal region with reduced cone reflectivity, abnormal outer retinal structures on SD-OCT, heterogeneous FAF, reduced CC perfusion and lower sensitivity compared to regions at greater eccentricities. Prior reports have shown wide variation in the location of the PRL among participants with macular diseases(Greenstein et al., 2008; Krishnan & Bedell, 2018; Messias et al., 2007; Rohrschneider et al., 2008; Timberlake et al., 2005; Verdina et al., 2017).

Cheung and Legge (Cheung & Legge, 2005) hypothesized that the location of the PRL could be function-driven, performance-driven or retinotopic-driven, defined as follows. A *function-driven* PRL describes placement of the PRL in the area of retina outside of the fovea that is most appropriate for a specific visual activity; for example, a superiorly located PRL may improve visual function for lower visual field tasks, such as reading or walking, by moving the scotoma into the upper visual field. PRLs have also been previously shown to shift dependent on the lighting conditions in participants with central scotoma by an average of 4.6^{o} and by as much as 12^{o} with a general shift to more superior retinal PRLs in low lighting conditions, like those used in this study(Trauzettel-Klosinski & Tornow, 1996). A *performance–driven* PRL describes placement of the PRL at the area of the retina that gives best visual acuity. A *retinotopic-driven* PRL describes a PRL located close to the edge of the macular atrophy that could best serve visual function based on retinotopic proximity to the anatomic fovea(Cheung & Legge, 2005). Note that these criteria are rarely mutually exclusive. In the present study, the PRL was located superior to the anatomic fovea, and adjacent to the edge of the macular atrophy in all 4 eyes (0.44-1.9 degrees from the fovea). The current manuscript supports the *function-driven* and *retinotopic-driven* criteria as the location of the PRL was located at the region superior to and closest to the anatomic fovea with

measurable visual function. We cannot conclude if the *performance-driven* criteria is met since, although the choice of PRL in our participants comes a cost to retinal sensitivity, we do not know how their choices compromise visual acuity (Shima et al., 2010).

4.5.2 RPE and Choriocapillaris abnormalities at the PRL

A homogenous distribution of fundus autofluorescence does not appear to be a strong criterion dictating the placement of the PRL. FAF showed heterogenous autofluorescence at the PRL in all 4 eyes (Figure 1). In 40122, 40146 and 40184, more normal-appearing FAF findings were present at greater eccentricities than the PRL, with 30014 showing more widespread FAF abnormalities. FAF abnormalities indicate RPE abnormalities which may result in the absence of wave-guiding cone outer segments and reduced sensitivities at the PRL.

Choriocapillaris (CC) flow does not appear to be a strong criterion dictating the placement of the PRL. CC flow was reduced at the PRL in participant 40184 with macular atrophy associated with cuticular drusen and participant 30014 with Stargardt disease but was within normal limits in participant 40146 with Best disease and 40122 with congenital rubella. In all participants, CC flow was closer to normal at increased eccentricities. Notably, in participant 40184, flow voids that were closer to normal could be found at similar eccentricities from the anatomic fovea as their chosen PRL. Flow voids in normal eyes have been reported as $10.31 \pm 3.66\%$(Q. Zhang et al., 2018). The differences in choriocapillaris flow voids observed among the 4 participants in the current study could reflect the variation in the pathogenic mechanisms and rate of progression of the 4 different diseases. The increased flow void in participants 40184 and 30014 suggest that choriocapillaris perfusion is more abnormal in Stargardt disease and macular degeneration associated with cuticular drusen than in congenital rubella (40122) and Best disease (40146). Prior studies have demonstrated impaired choriocapillaris blood flow within, around and beyond the margins of GA in non-neovascular AMD(Kvanta et al., 2017; Moreira-Neto et al., 2018; Moult et al., 2016; Sacconi et al., 2017), as we observed in 40184 and 30014.

4.5.3 Fixation differences with an Eccentric PRL

This study found a significant difference in BCEA between eccentric fixators and healthy participants, which is in line with previous studies comparing eccentric fixators to healthy age matched participants(Kumar & Chung, 2014). Interestingly, the BCEA increase may not be solely a result of eccentric fixation in our participants, as the BCEA in our eccentric fixation cohort was not significantly different from participants with RP that had central fixation. The lack of difference between eccentric and central fixators indicates that fixational stability may depend more on the number and health of the cones at the PRL than its location. The USH2A participants with visual acuity worse than 20/30 were the only RP group to be significantly different from normals, indicating that fixational instability may be related to visual acuity.

Previous studies have found an increase in fixational instability with increasing age and worsening visual acuity(Sheehy et al., 2020), but there was no such correlation found in this study. This is most likely due to lack of statistical power in our limited participant pool. The lack of correlation with age found in this study is an indication of including age-similar participants in each group.

4.5.4 Limitations

Our findings for relatively small PRL eccentricities from the fovea may inform, but should not be

extrapolated to predict structure and function of the PRL at greater eccentricities. Additionally, our results may not extend to foveal pathologies that are not included in the range of conditions studied here. Finally, the small number of study eyes means that we cannot rule out different behavior in individuals with the same retinal disease. That being said, we see strikingly common criteria being used for PRL selection in our cohort.

The alignment of all functional and structural data in this report is accurate, with the exception of MAIA fundus-guided microperimetry, which demonstrated measurable sensitivity values in regions of RPE and retinal atrophy shown by SD-OCT, FAF and AOSLO. This suggests potentially imprecise fundus localization of the visual stimulus using fundus-guided microperimetry. All functional testing modalities allow for the determination of the PRL in one eye at a time, and a different PRL may be used by each eye in binocular conditions where the better eye drives the location of the PRL(Tarita-Nistor et al., 2011).

Finally, BCEA measured in the AOSLO should not be directly compared with BCEA from the MAIA for several reasons. First, the fixation targets were different; the AOSLO used a small, blinking black dot in a red field, whereas the MAIA used a red circle 1 deg in diameter. Second, the AOSLO measured fixational eye movements over 5-second segments at 900 Hz while participants were instructed to fixate, whereas the MAIA BCEA was computed based on eye movements measured at 25 Hz over a much longer, continuous 10-minute period.

4.6 Conclusions

Individuals with central macular atrophy affecting the anatomic fovea adopt a new PRL that is structurally and functionally compromised in every measurable way: cone reflectivity/waveguiding, choriocapillaris perfusion, RPE health and retinal sensitivity are all worse at the PRL than at more peripheral locations. The two clear priorities in adopting an eccentric PRL are to position the PRL generally superior (nasal or temporal) to the anatomic fovea and close to the anatomic fovea. Assessing whether or not this is the best choice has not been determined and may prove difficult as participants have likely adapted to this new location.

Contents of this chapter are in prep for submission: Bensinger, E, Kolawole, O, Wong, J, Rinella, N, Foote KG, Zhou H, Sheehy C, Wang R, Roorda AJ, Duncan JL. High Resolution Imaging and Fixation Analysis of Eccentric Preferred Retinal Loci (PRL) in Macular Diseases

Table 4.1 Clinical characteristics of RP Participants and Macular Atrophy Participants. OD, right eye; OS, left eye; ARRP, autosomal recessive retinitis pigmentosa; BCVA, best corrected visual acuity. "None" indicates the participants did not undergo genetic testing.

ID	Study Eye	Disease	Mutations and Protein Effect	BCVA	Age	MAIA Sensitivity	Average BCEA
30014	OD	Stargardt disease	ABCA4 c.4457C>T, p.Pro1486Leu; c.3759; c.672ins6bp; c.672del32bp	20/40	26	-	0.07049
40184	OD	Cuticular drusen with macular atrophy	No disease causing genes	20/20	48	19	0.09213
40122	OS	Congenital Rubella	None	20/32	56	9	0.16362
40146	OS	Best vitelliform macular dystrophy	(BEST1 c. 920 C>T; p. Thr307Ile)	20/40	57	17	0.05375
40082	OS	ARRP Ush2A mutations	c.8522G>A, p.W2841X and c.11266G>A, p.G3756S	20/40	44	19	0.110
40151	OD	ARRP USH2A mutations	c.11864G>A, p.Trp3955* and c.6835G>C, p.Asp2279His	20/40	58	19	0.07986
40097	OS	USH2A	c.2299delG, p.Glu767SerfsX21 homozygous	20/32	34	-	0.062081
40153	OS	ARRP USH2A mutations	c.5299-?_5572+?del and c.9882C>G, p.Cys3294Trp	20/50	62	17	0.059405
40039	OS	ARRP USH2A mutations	c.2276G>T, p.Cys759Phe and c.2296T>C, p.Cys766Arg	20/16	48	26	0.083893
40180	OD	ARRP USH2A mutations	c.2299del, p.Glu767Serfs*21 and c.2276G>T, p.Cys759Phe	20/16	34	21	0.019893
40110	OD	ARRP USH2A mutations	c.11156G>A, p.Arg3719His and c.8659dup, p.Tyr2887Leufs*2	20/25	47	-	0.062788
40163	OD	ARRP USH2A mutations	c.2276G>T, p.Cys759Phe and c.1036A>C, p.N346H	20/16	49	25	0.093837
30019	OD	ARRP RHO mutations	c.152G>T p.Gly51Val	20/20	46	20	0.135981
40167	OD	ARRP RHO mutations	c.512C>G p.Ser270Arg	20/25	41	20	0.057845
40095	OS	ARRP RHO mutations	c.810C>A p.Ser270Arg	20/16	36	22	0.080229
40183	OS	ARRP RHO mutations	c.68C>A p.Pro23His	20/16	42	26	0.016133

REFERENCES

Aguilar, M., & Stiles, W. S. (1971). Saturation of the rod mechanism of the retina at high levels of stimulation. *Optica Acta*. https://doi.org/10.1080/09500347109696914

Anderson, D. H., Fisher, S. K., Erickson, P. A., & Tabor, G. A. (1980). Rod and cone disc shedding in the rhesus monkey retina: A quantitative study. *Experimental Eye Research*. https://doi.org/10.1016/0014-4835(80)90040-8

Arathorn, D. W., Yang, Q., Vogel, C. R., Zhang, Y., Tiruveedhula, P., & Roorda, A. (2007). Retinally stabilized cone-targeted stimulus delivery. *Optics Express*, *15*(21), 13731–13744. http://www.ncbi.nlm.nih.gov/pubmed/19550644

Bensinger, E., Rinella, N., Saud, A., Loumou, P., Ratnam, K., Griffin, S., Qin, J., Porco, T. C., Roorda, A., & Duncan, J. L. (2019). Loss of Foveal Cone Structure Precedes Loss of Visual Acuity in Patients With Rod-Cone Degeneration. *Investigative Ophthalmology and Visual Science*, *60*(8), 3187–3196. https://doi.org/10.1167/iovs.18-26245

Bensinger, E., Wang, Y., Ravikumar, S., Schmidt, B. P., & Roorda, A. (2018). Survey of transient hyporeflective clusters of cones in healthy eyes. *Investigative Ophthalmology & Visual Science*, *59*, 648.

Birch, D. G., Locke, K. G., Wen, Y., Locke, K. I., Hoffman, D. R., & Hood, D. C. (2013). Spectral-domain optical coherence tomography measures of outer segment layer progression in patients with X-linked retinitis pigmentosa. *JAMA Ophthalmology*. https://doi.org/10.1001/jamaophthalmol.2013.4160

Bittner, A. K., Ibrahim, M. A., Haythornthwaite, J. A., Diener-West, M., & Dagnelie, G. (2011). Vision test variability in retinitis pigmentosa and psychosocial factors. *Optometry and Vision Science*. https://doi.org/10.1097/OPX.0b013e3182348d0b

Boehm, A. E., Privitera, C. M., Schmidt, B. P., & Roorda, A. (2019). Transverse chromatic offsets with pupil displacements in the human eye: sources of variability and methods for real-time correction. *Biomedical Optics Express*, *10*(4), 1691. https://doi.org/10.1364/BOE.10.001691

Boll, F. (1876). Zur Anatomie and Physiologie der Retina. *Akad. d. Wissensch.*

Bowmaker, J. K., & Dartnall, H. J. (1980). Visual pigments of rods and cones in a human retina. *The Journal of Physiology*, *298*(1), 501–511. https://doi.org/10.1113/jphysiol.1980.sp013097

Bruce, K. S., Harmening, W. M., Langston, B. R., Tuten, W. S., Roorda, A., & Sincich, L. C. (2015). Normal perceptual sensitivity arising from weakly reflective cone photoreceptors. *Investigative Ophthalmology and Visual Science*, *56*(8), 4431–4438. https://doi.org/10.1167/iovs.15-16547

Burns, S. A., Elsner, A. E., Sapoznik, K. A., Warner, R. L., & Gast, T. J. (2019). Adaptive optics imaging of the human retina. *Progress in Retinal and Eye Research*, *68*(June), 1–30. https://doi.org/10.1016/j.preteyeres.2018.08.002

Carroll, J., Kay, D. B., Scoles, D., Dubra, A., & Lombardo, M. (2013). Adaptive optics retinal

imaging-clinical opportunities and challenges. *Current Eye Research*, *38*(7), 709–721. https://doi.org/10.3109/02713683.2013.784792

Charbel Issa, P., Gillies, M. C., Chew, E. Y., Bird, A. C., Heeren, T. F. C., Peto, T., Holz, F. G., & Scholl, H. P. N. (2013). Macular telangiectasia type 2. *Progress in Retinal and Eye Research*, *34*, 49–77. https://doi.org/10.1016/j.preteyeres.2012.11.002

Chen, M., Cooper, R. F., Han, G. K., Gee, J., Brainard, D. H., & Morgan, J. I. W. (2016). Multi-modal automatic montaging of adaptive optics retinal images. *Biomedical Optics Express*, *7*(12), 4899. https://doi.org/10.1364/boe.7.004899

Chen, Y., Roorda, A., & Duncan, J. L. (2010). Advances in imaging of Stargardt disease. *Advances in Experimental Medicine and Biology*. https://doi.org/10.1007/978-1-4419-1399-9_38

Cheung, S.-H., & Legge, G. E. (2005). Functional and cortical adaptations to central vision loss. *Visual Neuroscience*, *22*(02), 187–201. https://doi.org/10.1017/S0952523805222071

Clemons, T. E., Gillies, M. C., Chew, E. Y., Bird, A. C., Peto, T., Figueroa, M. J., & Harrington, M. W. (2010). Baseline characteristics of participants in the natural history study of macular telangiectasia (MacTel) MacTel project report No. 2. *Ophthalmic Epidemiology*, *17*(1), 66–73. https://doi.org/10.3109/09286580903450361

Cooper, R. F., Tuten, W. S., Dubra, A., Brainard, D. H., & Morgan, J. I. W. (2018). Non-invasive assessment of human cone photoreceptor function. *Biomedical Optics Express*, *9*(4), 1842. https://doi.org/10.1364/boe.9.001842

Crossland, M. D., Culham, L. E., Kabanarou, S. A., & Rubin, G. S. (2005). Preferred retinal locus development in patients with macular disease. *Ophthalmology*, *112*(9), 1579–1585. https://doi.org/10.1016/j.ophtha.2005.03.027

Curcio, C. A., Sloan, K. R., Kalina, R. E., & Hendrickson, A. E. (1990). Human photoreceptor topography. *Journal of Comparative Neurology*. https://doi.org/10.1002/cne.902920402

Domalpally, A., Danis, R. P., White, J., Narkar, A., Clemons, T., Ferris, F., & Chew, E. (2013). Circularity index as a risk factor for progression of geographic atrophy. *Ophthalmology*, *120*(12), 2666–2671. https://doi.org/10.1016/j.ophtha.2013.07.047

Duncan, J. L., Zhang, Y., Gandhi, J., Nakanishi, C., Othman, M., Branham, K. E. H., Swaroop, A., & Roorda, A. (2007). High-resolution imaging with adaptive optics in patients with inherited retinal degeneration. *Investigative Ophthalmology and Visual Science*, *48*(7), 3283–3291. https://doi.org/10.1167/iovs.06-1422

Enoch, J. M., & Birch, D. G. (1980). Evidence for Alteration in Photoreceptor Orientation. *Ophthalmology*. https://doi.org/10.1016/S0161-6420(80)35173-7

Erbezci, M., & Ozturk, T. (2017). Preferred Retinal Locus Locations in Age-Related Macular Degeneration. *Retina*, *38*(12), 2372–2378.

Ferris III, Frederick L, Kassoff, A., & Bailey, I. (1982). New visual acuity charts for clinical research. *American Journal of Ophthalmology*, *94*(1), 91–96. https://doi.org/10.1016/0002-9394(82)90197-0

Foote, K. G., Huerta, I., Gustafson, K., Baldwin, A., Zayit-Soudry, S., Rinella, N., Porco, T. C.,

& Roorda, A. (2019). Cone spacing correlates with retinal thickness and microperimetry in patients with inherited retinal degenerations. *Investigative Ophthalmology and Visual Science*, *60*(4), 1234–1243. https://doi.org/http://dx.doi.org/10.1167/iovs.18-25688

Foote, K. G., Loumou, P., Griffin, S., Qin, J., Ratnam, K., Porco, T. C., Roorda, A., & Duncan, J. L. (2018). Relationship between foveal cone structure and visual acuity measured with adaptive optics scanning laser ophthalmoscopy in retinal degeneration. *Investigative Ophthalmology and Visual Science*, *59*(8), 3385–3393. https://doi.org/10.1167/iovs.17-23708

Foote, K. G., Rinella, N., Tang, J., Bensaid, N., Zhou, H., Zhang, Q., Wang, R. K., Porco, T. C., Roorda, A., & Duncan, J. L. (2019). Cone structure persists beyond margins of short-wavelength autofluorescence in choroideremia. *Investigative Ophthalmology and Visual Science*, *60*(14), 4931–4942. https://doi.org/10.1167/iovs.19-27979

Foote, K. G., Wong, J. J., Boehm, A. E., Bensinger, E., Porco, T. C., Roorda, A., & Duncan, J. L. (2020). Comparing cone structure and function in Rho- And RPGR-associated retinitis pigmentosa. *Investigative Ophthalmology and Visual Science*, *61*(4). https://doi.org/10.1167/iovs.61.4.42

Geller, A. M., Sieving, P. A., & Green, D. G. (1992). Effect on grating identification of sampling with degenerate arrays. *Journal of the Optical Society of America A*. https://doi.org/10.1364/josaa.9.000472

Greenstein, V. C., Santos, R. A., Tsang, S. H., Smith, R. T., Barile, G. R., & Seiple, W. (2008). Preferred retinal locus in macular disease: characteristics and clinical implications. *Retina*, *28*(9), 1234–1240. https://doi.org/10.1097/IAE.0b013e31817c1b47

Grieve, K., Tiruveedhula, P., Zhang, Y., & Roorda, A. (2006). Multi-wavelength imaging with the adaptive optics scanning laser Ophthalmoscope. *Optics Express*, *14*(25), 12230. https://doi.org/10.1364/oe.14.012230

Guevara-Torres, A., Williams, D. R., & Schallek, J. B. (2020). Origin of cell contrast in offset aperture adaptive optics ophthalmoscopy. *Optics Letters*, *45*(4), 840. https://doi.org/10.1364/ol.382589

Hamel, C. P. (2007). Cone rod dystrophies. *Orphanet Journal of Rare Diseases*. https://doi.org/10.1186/1750-1172-2-7

Hariri, A. H., Zhang, H. Y., Ho, A., Francis, P., Weleber, R. G., Birch, D. G., Ferris, F. L., Sadda, S. V. R., Bernstein, P. S., Heckenlively, J., Iannaccone, A., Lam, B., Pennesi, M. E., Chiostri, J., Erker, L. R., Wilson, D. J., & McCormack, J. B. (2016). Quantification of ellipsoid zone changes in retinitis pigmentosa using en face spectral domain-optical coherence tomography. *JAMA Ophthalmology*. https://doi.org/10.1001/jamaophthalmol.2016.0502

Harmening, W. M., Tuten, W. S., Roorda, A., & Sincich, L. C. (2014). Mapping the Perceptual Grain of the Human Retina. *Journal of Neuroscience*, *34*(16), 5667–5677. https://doi.org/10.1523/jneurosci.5191-13.2014

Harmening, Wolf M., Tiruveedhula, P., Roorda, A., & Sincich, L. C. (2012). Measurement and correction of transverse chromatic offsets for multi-wavelength retinal microscopy in the

living eye. *Biomedical Optics Express*, *3*(11), 2772. https://doi.org/10.1364/boe.3.002772

Hartong, D. T., Berson, E. L., & Dryja, T. P. (2006). Retinitis pigmentosa. In *Lancet*. https://doi.org/10.1016/S0140-6736(06)69740-7

Holopigian, K., Greenstein, V., Seiple, W., & Carr, R. E. (1996). Rates of change differ among measures of visual function in patients with retinitis pigmentosa. *Ophthalmology*. https://doi.org/10.1016/S0161-6420(96)30679-9

Hood, D. C., Lin, C. E., Lazow, M. A., Locke, K. G., Zhang, X., & Birch, D. G. (2009). Thickness of receptor and post-receptor retinal layers in patients with retinitis pigmentosa measured with frequency-domain optical coherence tomography. *Investigative Ophthalmology and Visual Science*. https://doi.org/10.1167/iovs.08-2936

Hood, D. C., Ramachandran, R., Holopigian, K., Lazow, M., Birch, D. G., & Greenstein, V. C. (2011). Method for deriving visual field boundaries from OCT scans of patients with retinitis pigmentosa. *Biomedical Optics Express*. https://doi.org/10.1364/boe.2.001106

Jonnal, R. S., Kocaoglu, O. P., Zawadzki, R. J., Lee, S. H., Werner, J. S., & Miller, D. T. (2014). The cellular origins of the outer retinal bands in optical coherence tomography images. *Investigative Ophthalmology and Visual Science*, *55*(12), 7904–7918. https://doi.org/10.1167/iovs.14-14907

Jonnal, R. S., Rha, J., Zhang, Y., Cense, B., Gao, W., & Miller, D. T. (2007). In vivo functional imaging of human cone photoreceptors. *Optics Express*, *15*(24), 16141. https://doi.org/10.1364/oe.15.016141

Joseph, A., Parkins, K., Yang, Q., Guevara-Torres, A., & Schallek, J. (2018). Real-time quantification of single blood-cell velocity in living human and mouse eye using adaptive optics. *Investigative Ophthalmology and Visual Science*, *59*(9), 1973.

Kilpeläinen, M., Putnam, N. M., Ratnam, K., & Roorda, A. (2020). The Anatomical, Functional and Perceived Location of the Fovea in the Human Visual System. *Cell Press Sneak Peak*, 1–22. https://doi.org/10.2139/ssrn.3699785

Kocaoglu, O. P., Lee, S., Jonnal, R. S., Wang, Q., Herde, A. E., Derby, J. C., Gao, W., & Miller, D. T. (2011). Imaging cone photoreceptors in three dimensions and in time using ultrahigh resolution optical coherence tomography with adaptive optics. *Biomedical Optics Express*, *2*(4), 748. https://doi.org/10.1364/boe.2.000748

Krishnan, A. K., & Bedell, H. E. (2018). Functional changes at the preferred retinal locus in subjects with bilateral central vision loss. *Graefe's Archive for Clinical and Experimental Ophthalmology*, *256*(1), 29–37. https://doi.org/10.1007/s00417-017-3818-3

Kumar, G., & Chung, S. T. L. (2014). Characteristics of Fixational Eye Mov ements in People With Macular Disease. *Investigative Ophthalmology & Visual Science*, *55*(8), 5125–5133. https://doi.org/10.1167/iovs.14-14608

Kvanta, A., Casselholm de Salles, M., Amrén, U., & Bartuma, H. (2017). Optical Coherence Tomography Angiography of the Foveal Microvasculature in Geographic Atrophy. *Retina*, *37*(5), 936–942. https://doi.org/10.1097/IAE.0000000000001248

Landa, G., Gentile, R. C., Garcia, P. M. T., Muldoon, T. O., & Rosen, R. B. (2012). External

limiting membrane and visual outcome in macular hole repair: Spectral domain OCT analysis. *Eye*, *26*(1), 61–69. https://doi.org/10.1038/eye.2011.237

Langlo, C. S., Patterson, E. J., Higgins, B. P., Summerfelt, P., Razeen, M. M., Erker, L. R., Parker, M., Collison, F. T., Fishman, G. A., Kay, C. N., Zhang, J., Weleber, R. G., Yang, P., Wilson, D. J., Pennesi, M. E., Lam, B. L., Chiang, J., Chulay, J. D., Dubra, A., … Carroll, J. (2016). Residual foveal cone structure in CNGB3-associated achromatopsia. *Investigative Ophthalmology and Visual Science*, *57*(10), 3984–3995. https://doi.org/10.1167/iovs.16-19313

Li, K. Y., Tiruveedhula, P., & Roorda, A. (2010). Intersubject variability of foveal cone photoreceptor density in relation to eye length. *Investigative Ophthalmology and Visual Science*. https://doi.org/10.1167/iovs.10-5499

Liang, J., Williams, D. R., & Miller, D. T. (1997). Supernormal vision and high-resolution retinal imaging through adaptive optics. *Journal of the Optical Society of America A*, *14*(11), 2884. https://doi.org/10.1364/josaa.14.002884

Liao, W., Rohr, K., & Wörz, S. (2013). Globally optimal curvature-regularized fast marching for vessel segmentation. *Lecture Notes in Computer Science (Including Subseries Lecture Notes in Artificial Intelligence and Lecture Notes in Bioinformatics)*, *8149 LNCS*(PART 1), 550–557. https://doi.org/10.1007/978-3-642-40811-3_69

Litts, K. M., Okada, M., Heeren, T. F. C., Kalitzeos, A., Rocco, V., Mastey, R. R., Singh, N., Kane, T., Kasilian, M., Fruttiger, M., Michaelides, M., Carroll, J., & Egan, C. (2020). Longitudinal Assessment of Remnant Foveal Cone Structure in a Case Series of Early Macular Telangiectasia Type 2. *Translational Vision Science & Technology*, *9*(4), 27. https://doi.org/10.1167/tvst.9.4.27

MAIA. (2011). *Macular Integrity Assessment Operating Manual*.

Marcos, S., Burns, S. A., & He, J. C. (1998). Model for cone directionality reflectometric measurements based on scattering. *Journal of the Optical Society of America A*. https://doi.org/10.1364/josaa.15.002012

Masella, B. D., Hunter, J. J., & Williams, D. R. (2014). New wrinkles in retinal densitometry. *Investigative Ophthalmology and Visual Science*, *55*(11), 7525–7534. https://doi.org/10.1167/iovs.13-13795

Meadway, A., McKeown, A. S., Samuels, B. C., & Sincich, L. C. (2020). Life Cycle and Lensing of a Macular Microcyst. *Ophthalmic Research*, *63*(4), 383–391. https://doi.org/10.1159/000505785

Meadway, A., & Sincich, L. C. (2018). Light propagation and capture in cone photoreceptors. *Biomedical Optics Express*, *9*(11), 5543. https://doi.org/10.1364/boe.9.005543

Meadway, A., & Sincich, L. C. (2019). Light reflectivity and interference in cone photoreceptors. *Biomedical Optics Express*, *10*(12), 6531. https://doi.org/10.1364/boe.10.006531

Merino, D., Duncan, J. L., Tiruveedhula, P., & Roorda, A. (2011). Observation of cone and rod photoreceptors in normal subjects and patients using a new generation adaptive optics scanning laser ophthalmoscope. *Biomedical Optics Express*.

https://doi.org/10.1364/boe.2.002189

Messias, A., Reinhard, J., Cruz, A. A. V., Dietz, K., MacKeben, M., & Trauzettel-Klosinski, S. (2007). Eccentric fixation in Stargardt's disease assessed by Tubingen perimetry. *Investigative Ophthalmology & Visual Science*, *48*(12), 5815–5822. https://doi.org/10.1167/iovs.06-0367

Moreira-Neto, C. A., Moult, E. M., Fujimoto, J. G., Waheed, N. K., & Ferrara, D. (2018). Choriocapillaris loss in advanced age-related macular degeneration. *Journal of Ophthalmology*, *2018*. https://doi.org/10.1155/2018/8125267

Morgan, J. I. W., Han, G., Klinman, E., Maguire, W. M., Chung, D. C., Maguire, A. M., & Bennett, J. (2014). High-resolution adaptive optics retinal imaging of cellular structure in choroideremia. *Investigative Ophthalmology and Visual Science*, *55*(10), 6381–6397. https://doi.org/10.1167/iovs.13-13454

Moult, E.M., Waheed, N.K., Novais, E.A., Choi, W., Lee, B., Ploner, S.B., Cole, E. D., & Louzada, R.N., Lu, C.D., Rosenfeld, P.J., Duker, J.S., Fujimoto, J. G. (2016). Swept- source optical coherence tomography angiography reveals choriocapillaris alterations in eyes with nascent geographic atrophy and drusen-associated geography atrophy. *Retina*, *36*, 2–11.

Mozaffari, S., LaRocca, F., Jaedicke, V., Tiruveedhula, P., & Roorda, A. (2020). Wide-vergence, multi-spectral adaptive optics scanning laser ophthalmoscope with diffraction-limited illumination and collection. *Biomedical Optics Express*, *11*(3), 1617. https://doi.org/10.1364/boe.384229

Mukherjee, D., Lad, E. M., Vann, R. R., Jaffe, S. J., Clemons, T. E., Friedlander, M., Chew, E. Y., Jaffe, G. J., & Farsiu, S. (2017). Correlation Between Macular Integrity Assessment and Optical Coherence Tomography Imaging of Ellipsoid Zone in Macular Telangiectasia Type 2. *Investigative Ophthalmology & Visual Science*, *58*(6), BIO291–BIO299. https://doi.org/10.1167/iovs.17-21834

Pallikaris, A., Williams, D. R., & Hofer, H. (2003). The reflectance of single cones in the living human eye. *Investigative Ophthalmology and Visual Science*, *44*(10), 4580–4592. https://doi.org/10.1167/iovs.03-0094

Parodi, M. B., Triolo, G., Morales, M., Ng, M. E., Borrelli, E., Cicinelli, M. V, Cascavilla, M. L., & Bandello, F. (2015). MP1 and MAIA fundus perimetry in healthy subjects and patients affected by retinal dystrophies. *Retina*, *35*(8), 1662–1669.

Peng, D., Merriman, B., Osher, S., Zhao, H., & Kang, M. (1999). A PDE-Based Fast Local Level Set Method. *Journal of Computational Physics*. https://doi.org/10.1006/jcph.1999.6345

Pircher, M., Zawadzki, R. J., Evans, J. W., Werner, J. S., & Hitzenberger, C. K. (2008). Simultaneous imaging of human cone mosaic with adaptive optics enhanced scanning laser ophthalmoscopy and high-speed transversal scanning optical coherence tomography. *Optics Letters*. https://doi.org/10.1364/ol.33.000022

Poonja, S., Patel, S., Henry, L., & Roorda, A. (2005). Dynamic visual stimulus presentation in an adaptive optics scanning laser ophthalmoscope. *Journal of Refractive Surgery*, *21*(5), S575–S580. https://doi.org/10.1364/FIO.2004.FThV3

Powner, M. B., Gillies, M. C., Tretiach, M., Scott, A., Guymer, R. H., Hageman, G. S., &

Fruttiger, M. (2010). Perifoveal Müller Cell Depletion in a Case of Macular Telangiectasia Type 2. *Ophthalmology*, *117*(12), 2407–2416. https://doi.org/10.1161/CIRCULATIONAHA.110.956839

Powner, M. B., Gillies, M. C., Zhu, M., Vevis, K., Hunyor, A. P., & Fruttiger, M. (2013). Loss of Müller's cells and photoreceptors in macular telangiectasia type 2. *Ophthalmology*, *120*(11), 2344–2352. https://doi.org/10.1016/j.ophtha.2013.04.013

Putnam, N. M., Hammer, D. X., Zhang, Y., Merino, D., & Roorda, A. (2010). Modeling the foveal cone mosaic imaged with adaptive optics scanning laser ophthalmoscopy. *Optics Express*. https://doi.org/10.1364/oe.18.024902

Putnam, N. M., Hofer, H. J., Doble, N., Chen, L., Carroll, J., & Williams, D. R. (2005). The locus of fixation and the foveal cone mosaic. *Journal of Vision*, *5*(7), 632–939. https://doi.org/10.1167/5.7.3

Randerson, E. L., Davis, D., Higgins, B., Kim, J. E., Han, D. P., Connor, T. B., Wirostko, W. J., & Carroll, J. (2015). Assessing Photoreceptor Structure in Macular Hole using Split-detector Adaptive Optics Scanning Light Ophthalmoscopy. *European Ophthalmic Review*, *09*(01), 59. https://doi.org/10.17925/eor.2015.09.01.59

Ratnam, K., Carroll, J., Porco, T. C., Duncan, J. L., & Roorda, A. (2013). Relationship between foveal cone structure and clinical measures of visual function in patients with inherited retinal degenerations. *Investigative Ophthalmology and Visual Science*. https://doi.org/10.1167/iovs.13-12557

Reiniger, J. L., Domdei, N., Linden, M., Holz, F. G., & Wolf, M. H. (2019). Relationship between the foveal photoreceptor mosaic and adaptive optics corrected visual acuity. *Investigative Ophthalmology and Visual Science*, *60*(9), 1777.

Rodieck, R. W. (1991). The density recovery profile: A method for the analysis of points in the plane applicable to retinal studies. *Visual Neuroscience*, *6*(2), 95–111. https://doi.org/10.1017/S095252380001049X

Rohrschneider, K., Bültmann, S., & Springer, C. (2008). Use of fundus perimetry (microperimetry) to quantify macular sensitivity. *Progress in Retinal and Eye Research*, *27*(5), 536–548. https://doi.org/10.1016/j.preteyeres.2008.07.003

Roorda, A., & Duncan, J. L. (2015). Adaptive Optics Ophthalmoscopy. *Annual Review of Vision Science*. https://doi.org/10.1146/annurev-vision-082114-035357

Roorda, A., Romero-Borja, F., Donnelly III, W. J., Queener, H., Hebert, T. J., & Campbell, M. C. (2002). Adaptive Optics Scanning Laser Ophthalmoscopy (AOSLO). *Biomedical Optics Express*, *10*(9), 405–412.

Roorda, A., & Williams, D. R. (1999). The arrangement of the three cone classes in the living human eye. *Nature*, *397*, 520–522.

Roorda, A., & Williams, D. R. (2002). Optical fiber properties of individual human cones. *Journal of Vision*, *2*(5), 404–412. https://doi.org/10.1167/2.5.4

Roorda, A., Zhang, Y., & Duncan, J. L. (2007). High-resolution in vivo imaging of the RPE mosaic in eyes with retinal disease. *Investigative Ophthalmology and Visual Science*, *48*(5),

2297–2303. https://doi.org/10.1167/iovs.06-1450

Rosenfeld, P. J., Durbin, M. K., Roisman, L., Zheng, F., Miller, A., Robbins, G., Schaal, K. B., & Gregori, G. (2016). ZEISS Angioplex^{TM} Spectral Domain Optical Coherence Tomography Angiography: Technical Aspects. *Developments in Ophthalmology*, *56*, 18–29. https://doi.org/10.1159/000442773

Rossi, E. A., Chung, M., Dubra, A., Hunter, J. J., Merigan, W. H., & Williams, D. R. (2011). Imaging retinal mosaics in the living eye. *Eye*. https://doi.org/10.1038/eye.2010.221

Rossi, Ethan A., Granger, C. E., Sharma, R., Yang, Q., Saito, K., Schwarz, C., Walters, S., Nozato, K., Zhang, J., Kawakami, T., Fischer, W., Latchney, L. R., Hunter, J. J., Chung, M. M., & Williams, D. R. (2017). Imaging individual neurons in the retinal ganglion cell layer of the living eye. *Proceedings of the National Academy of Sciences of the United States of America*, *114*(3), 586–591. https://doi.org/10.1073/pnas.1613445114

Sacconi, R., Eleonora, C., Carnevali, A., Querques, L., Bandello, F., & Querques, G. (2017). Optical Coherence Tomography Angiography in Geographic Atrophy. *Retina*, *0*(5), 1–6. https://doi.org/10.1097/IAE.0000000000001248

Sallo, F. B., Peto, T., Egan, C., Wolf-Schnurrbusch, U. E. K., Clemons, T. E., Gillies, M. C., Pauleikhoff, D., Rubin, G. S., Chew, E. Y., & Bird, A. C. (2012). "En face" OCT imaging of the IS/OS junction line in type 2 idiopathic macular telangiectasia. *Investigative Ophthalmology and Visual Science*, *53*(10), 6145–6152. https://doi.org/10.1167/iovs.12-10580

Sallo, F. B., Peto, T., Egan, C., Wolf-Schnurrbusch, U. E. K., Clemons, T. E., Gillies, M. C., Pauleikhoff, D., Rubin, G. S., Chew, E. Y., Bird, A. C., Sahel, J. A., Guymer, R., Soubrane, G., Gaudric, A., Schwartz, S., Constable, I., Cooney, M., Egan, C., Singerman, L., … Miller, J. W. (2012). The IS/OS junction layer in the natural history of type 2 idiopathic macular telangiectasia. *Investigative Ophthalmology and Visual Science*, *53*(12), 7889–7895. https://doi.org/10.1167/iovs.12-10765

Scoles, D., Flatter, J. A., Cooper, R. F., Langlo, C. S., Robison, S., Neitz, M., Weinberg, D. V., Pennesi, M. E., Han, D. P., Dubra, A., & Carroll, J. (2016). Assessing photoreceptor structure associated with ellipsoid zone disruptions visualized with optical coherence tomography. *Retina*, *36*(1), 91–103. https://doi.org/10.1097/IAE.0000000000000618.Assessing

Scoles, D., Sulai, Y. N., Langlo, C. S., Fishman, G. A., Curcio, C. A., Carroll, J., & Dubra, A. (2014). In Vivo Imaging of Human Cone Photoreceptor Inner Segments. *Investigative Ophthalmology and Visual Science*, *55*(7), 4244–4251. https://doi.org/10.1167/iovs.14-14542

Sheehy, C. K., Bensinger, E. S., Romeo, A., Rani, L., Stepien-bernabe, N., Shi, B., Helft, Z., Putnam, N., Cordano, C., Gelfand, J. M., Bove, R., Stevenson, S. B., & Green, A. J. (2020). Fixational microsaccades : A quantitative and objective measure of disability in multiple sclerosis. *Multiple Sclerosis Journal*, 343–353. https://doi.org/10.1177/1352458519894712

Shima, N., Markowitz, S. N., & Reyes, S. V. (2010). Concept of a functional retinal locus in age-related macular degeneration. *Canadian Journal of Ophthalmology*, *45*(1), 62–66.

https://doi.org/10.3129/i09-236

Smith, T. B., Parker, M., Steinkamp, P. N., Weleber, R. G., Smith, N., Wilson, D. J., Bernstein, P. S., Birch, D. G., Chiostri, J., Erker, L. R., Heckenlively, J. R., Iannaccone, A., Lam, B. L., McCormack, J. B., Pennesi, M. E., Ferris, F. L., Francis, P. J., Ho, A., Sadda, S. R., … Zilliox, P. (2016). Structure-Function Modeling of Optical Coherence Tomography and Standard Automated Perimetry in the Retina of Patients with Autosomal Dominant Retinitis Pigmentosa. *PLoS ONE*. https://doi.org/10.1371/journal.pone.0148022

Song, H., Rossi, E. A., Latchney, L., Bessette, A., Stone, E., Hunter, J. J., Williams, D. R., & Chung, M. (2015). Cone and rod loss in stargardt disease revealed by adaptive optics scanning light ophthalmoscopy. *JAMA Ophthalmology*, *133*(10), 1198–1203. https://doi.org/10.1001/jamaophthalmol.2015.2443

Song, H., Rossi, E. A., Stone, E., Latchney, L., Williams, D., Dubra, A., & Chung, M. (2018). Phenotypic diversity in autosomal-dominant cone-rod dystrophy elucidated by adaptive optics retinal imaging. *The British Journal of Ophthalmology*, *102*(1), 136–141. https://doi.org/10.1136/bjophthalmol-2017-310498

Stevenson, S. B., & Roorda, A. (2005). Correcting for miniature eye movements in high resolution scanning laser ophthalmoscopy. *Ophthalmic Technologies XV*, *5688*, 145. https://doi.org/10.1117/12.591190

Sullivan, L. S., Bowne, S. J., Reeves, M. J., Blain, D., Goetz, K., Difor, V. N., Vitez, S., Wang, X., Tumminia, S. J., & Daiger, S. P. (2013). Prevalence of mutations in eyeGENE probands with a diagnosis of autosomal dominant retinitis pigmentosa. *Investigative Ophthalmology and Visual Science*, *54*(9), 6255–6261. https://doi.org/10.1167/iovs.13-12605

Sun, L. W., Johnson, R. D., Langlo, C. S., Cooper, R. F., Razeen, M. M., Russillo, M. C., Dubra, A., Connor, T. B., Han, D. P., Pennesi, M. E., Kay, C. N., Weinberg, D. V., Stepien, K. E., & Carroll, J. (2016). Assessing photoreceptor structure in retinitis pigmentosa and usher syndrome. *Investigative Ophthalmology and Visual Science*, *57*(6), 2428–2442. https://doi.org/10.1167/iovs.15-18246

Syed, R., Sundquist, S. M., Ratnam, K., Zayit-Soudry, S., Zhang, Y., Brooks Crawford, J., MacDonald, I. M., Godara, P., Rha, J., Carroll, J., Roorda, A., Stepien, K. E., & Duncan, J. L. (2013). High-resolution images of retinal structure in patients with choroideremia. *Investigative Ophthalmology and Visual Science*, *54*(2), 950–961. https://doi.org/10.1167/iovs.12-10707

Talcott, K. E., Ratnam, K., Sundquist, S. M., Lucero, A. S., Lujan, B. J., Tao, W., Porco, T. C., Roorda, A., & Duncan, J. L. (2011). Longitudinal study of cone photoreceptors during retinal degeneration and in response to ciliary neurotrophic factor treatment. *Investigative Ophthalmology and Visual Science*. https://doi.org/10.1167/iovs.10-6479

Tarita-Nistor, L., Brent, M. H., Steinbach, M. J., & González, E. G. (2011). Fixation stability during binocular viewing in patients with age-related macular degeneration. *Investigative Ophthalmology and Visual Science*, *52*(3), 1887–1893. https://doi.org/10.1167/iovs.10-6059

Timberlake, G. T., Mainsrer, M. A., Peli, E., Augliere, R. A., Essock, E. A., & Arend, L. E. (1986). Reading With a Macular Scotoma. *Investigative Ophthalmology and Visual Science*,

27, 1137–1147.

Timberlake, G. T., Sharma, M. K., Grose, S. A., Gobert, D. V, Gauch, J. M., & Maino, J. H. (2005). Retinal location of the preferred retinal locus relative to the fovea in scanning laser ophthalmoscope images. *Optometry and Vision Science*, *82*(3), 177–185. https://doi.org/10.1097/01.OPX.0000156311.49058.C8

Trauzettel-Klosinski, S., & Tornow, R. P. (1996). Fixation behavior and reading ability in macular scotoma. Assessed by Tuebingen manual perimetry and scanning laser ophthalmoscopy. *Neuro-Ophthalmology*, *16*(4), 241–253. https://doi.org/10.3109/01658109609044632

Tu, J. H., Foote, K. G., Lujan, B. J., Ratnam, K., Qin, J., Gorin, M. B., Cunningham, E. T., Tuten, W. S., Duncan, J. L., & Roorda, A. (2017). Dysflective cones: Visual function and cone reflectivity in long-term follow-up of acute bilateral foveolitis. *American Journal of Ophthalmology Case Reports*, *7*, 14–19. https://doi.org/10.1016/j.ajoc.2017.04.001

Tuten, W., Tiruveedhula, P., & Roorda, A. (2012). Adaptive Optics Scanning Laser Ophthalmoscope-Based Microperimetry. *Optometry and Vision Science*, *89*(5), 563–574.

Verdina, T., Greenstein, V. C., Sodi, A., Tsang, S. H., Burke, T. R., Passerini, I., Allikmets, R., Virgili, G., Cavallini, G. M., & Rizzo, S. (2017). Multimodal analysis of the Preferred Retinal Location and the Transition Zone in patients with Stargardt Disease. *Graefe's Archive for Clinical and Experimental Ophthalmology*, *255*(7), 1307–1317. https://doi.org/10.1007/s00417-017-3637-6

Wald, G. (1955). The molecular basis of visual excitation. *Science in Progress, Series 9*, 133–160.

Wang, Q., Tuten, W. S., Lujan, B. J., Holland, J., Bernstein, P. S., Schwartz, S. D., Duncan, J. L., & Roorda, A. (2015). Adaptive optics microperimetry and OCT images show preserved function and recovery of cone visibility in macular telangiectasia type 2 retinal lesions. *Investigative Ophthalmology and Visual Science*, *56*(2), 778–786. https://doi.org/10.1167/iovs.14-15576

Wang, Y., Bensaid, N., Tiruveedhula, P., Ma, J., Ravikumar, S., & Roorda, A. (2019). Human foveal cone photoreceptor topography and its dependence on eye length. *ELife*. https://doi.org/10.7554/elife.47148

Watson, A. B., & Pelli, D. G. (1983). Quest: A Bayesian adaptive psychometric method. *Perception & Psychophysics*, *33*(2), 113–120. https://doi.org/10.3758/BF03202828

Webb, R. H., Hughes, G. W., & Delori, F. C. (1987). Confocal Scanning Laser Ophthalmoscope. *Applied Optics*, *26*(8), 1492–1499. https://doi.org/10.5005/jp/books/11266_39

Westheimer, G. (2008). Directional sensitivity of the retina: 75 Years of Stiles-Crawford effect. In *Proceedings of the Royal Society B: Biological Sciences*. https://doi.org/10.1098/rspb.2008.0712

Wilk, M. A., Dubis, A. M., Cooper, R. F., Summerfelt, P., Dubra, A., & Carroll, J. (2017). Assessing the spatial relationship between fixation and foveal specializations. *Vision Research*, *132*, 53–61. https://doi.org/10.1016/j.visres.2016.05.001

Wolfing, J. I., Chung, M., Carroll, J., Roorda, A., & Williams, D. R. (2006). High-Resolution Retinal Imaging of Cone-Rod Dystrophy. *Ophthalmology*. https://doi.org/10.1016/j.ophtha.2006.01.056

Wright, A. F., Chakarova, C. F., Abd El-Aziz, M. M., & Bhattacharya, S. S. (2010). Photoreceptor degeneration: Genetic and mechanistic dissection of a complex trait. *Nature Reviews Genetics*, *11*(4), 273–284. https://doi.org/10.1038/nrg2717

Zayit-Soudry, S., Duncan, J. L., Syed, R., Menghini, M., & Roorda, A. J. (2013). Cone structure imaged with adaptive optics scanning laser ophthalmoscopy in eyes with nonneovascular age-related macular degeneration. *Investigative Ophthalmology and Visual Science*. https://doi.org/10.1167/iovs.13-12433

Zayit-Soudry, S., Sippl-Swezey, N., Porco, T. C., Lynch, S. K., Syed, R., Ratnam, K., Menghini, M., Roorda, A. J., & Duncan, J. L. (2015). Repeatability of cone spacing measures in eyes with inherited retinal degenerations. *Investigative Ophthalmology and Visual Science*. https://doi.org/10.1167/iovs.15-17010

Zhang, F., Kurokawa, K., Lassoued, A., Crowell, J. A., & Miller, D. T. (2019). Cone photoreceptor classification in the living human eye from photostimulation-induced phase dynamics. *Proceedings of the National Academy of Sciences of the United States of America*, *116*(16), 7951–7956. https://doi.org/10.1073/pnas.1816360116

Zhang, Q., Zheng, F., Motulsky, E. H., Gregori, G., Chu, Z., Chen, C. L., Li, C., De Sisternes, L., Durbin, M., Rosenfeld, P. J., & Wang, R. K. (2018). A novel strategy for quantifying choriocapillaris flow voids using swept-source OCT angiography. *Investigative Opthalmology & Visual Science*, *59*(1), 203–211. https://doi.org/10.1167/iovs.17-22953

Zhang, T., Godara, P., Blanco, E. R., Griffin, R. L., Wang, X., Curcio, C. A., & Zhang, Y. (2015). Variability in Human Cone Topography Assessed by Adaptive Optics Scanning Laser Ophthalmoscopy. *American Journal of Ophthalmology*. https://doi.org/10.1016/j.ajo.2015.04.034

Zur, D., & Ullman, S. (2003). Filling-in of retinal scotomas. *Vision Research*, *43*(9), 971–982. https://doi.org/10.1016/S0042-6989(03)00038-5